

(1959).

¹⁷R. H. Dalitz and B. W. Downs, *Phys. Rev.* **111**, 967 (1958).¹⁸M. M. Block, in *Proceedings of the International Conference on Hyperfragments, St. Cergue, 1963* (CERN, Geneva, 1964), p. 75.¹⁹R. C. Herndon and Y. C. Tang, *Phys. Rev.* **159**, 853 (1967). This paper is part of a series including *Phys. Rev.* **165**, 1093 (1968) and *Phys. Rev.* **153**, 1091 (1967). For a recent summary, see Y. C. Tang, in *Proceedings of International Conference on Hypernuclear Physics*, edited by A. R. Bodmer and L. G. Hyman (ANL, Argonne, Ill., 1969), p. 276.²⁰A. Bamberger, M. A. Faessler, U. Lynen, H. Prekarz, J. Piekarz, J. Pniewski, B. Povh, H. G. Ritter, and V. Soergel, *Phys. Letters* **36B**, 412 (1971).²¹K. Bunnell, M. Derrick, T. Fields, L. G. Hyman, and G. Keyes, *Phys. Rev. D* **2**, 98 (1970).²²P. A. Katz, K. Bunnell, M. Derrick, T. Fields, L. G. Hyman, and G. Keyes, *Phys. Rev. D* **1**, 1267 (1970).²³Mason B. Watson, Massimiliano Ferro-Luzzi, and Robert D. Tripp, *Phys. Rev.* **131**, 2248 (1963).²⁴H. Courant, H. Filthuth, P. Franzini, R. G. Glasser, A. Minguzzi-Ranzi, A. Segar, W. Willis, R. A. Burnstein, T. B. Day, B. Kehoe, A. J. Herz, M. Sakitt, B. Sechi-Zorn, N. Seeman, and G. A. Snow, *Phys. Rev. Letters* **10**, 409 (1963).²⁵G. Bohm, J. Klabuhn, U. Kreckler, F. Wysotski, G. Coremans, W. Gajewski, C. Mayeur, J. Sacton, P. Vilain, G. Wilquet, D. O'Sullivan, D. Stanley, D. H. Davis, E. R. Fletcher, S. P. Lovell, N. C. Roy, J. H. Wickens, A. Filipkowski, K. Garbowska-Pniewska, T. Pniewski, E. Skrzypczak, T. Sobczak, J. E. Allen, V. A. Bull, A. P. Conway, A. Fishwick, and P. V. March, *Nucl. Phys.* **B4**, 511 (1968).²⁶G. Bohm, U. Kreckler, C. Mayeur, J. Sacton, J. H. Wickens, F. Esmael, D. Stanley, D. H. Davis, J. E. Allen, A. Filipkowski, and E. Skrzypczak, *Nuovo Cimento* **70A**, 384 (1970).²⁷D. Bertrand, G. Coremans, C. Mayeur, J. Sacton, P. Vilain, G. Wilquet, J. H. Wickens, D. O'Sullivan, D. H. Davis, and J. E. Allen, *Nucl. Phys.* **B16**, 77 (1970). This paper also contains references to earlier results.²⁸R. H. Dalitz and L. Liu, *Phys. Rev.* **116**, 1312 (1959).²⁹B. Cork, L. Kerth, W. Wentzel, J. Cronin, and R. Cool, *Phys. Rev.* **120**, 1000 (1960); S. Olsen, L. Pondrom, R. Handler, P. Limon, J. A. Smith, and O. E. Overseth, *Phys. Rev. Letters* **24**, 843 (1970).³⁰O. E. Overseth and R. F. Roth, *Phys. Rev. Letters* **19**, 391 (1967).³¹R. G. Ammar, *Nuovo Cimento* **14**, 1226 (1959).³²R. H. Dalitz, private communication.³³B. W. Downs and R. J. N. Phillips, *Nuovo Cimento* **41**, 374 (1966).

Production of Charged Pions by 730-MeV Protons from Hydrogen and Selected Nuclei*

D. R. F. Cochran, P. N. Dean, P. A. M. Gram, E. A. Knapp, E. R. Martin,

D. E. Nagle, R. B. Perkins, W. J. Schlaer, H. A. Thiessen, and E. D. Theriot†
University of California Los Alamos Scientific Laboratory, Los Alamos, New Mexico 87544

(Received 14 February 1972)

An experiment was done in the external proton beam of the Berkeley 184-in. cyclotron to measure the production cross sections for pions from various target nuclei, from hydrogen to lead. The cross-section data are presented and the reaction mechanisms discussed. The hydrogen production appears to fit the one-pion-exchange model.

I. INTRODUCTION

Pion production cross sections for protons on hydrogen and other nuclei constitute some of the basic data for medium-energy physics, equally important in the theoretical understanding of pion physics and as input for the design of pion beams for the new generation of meson factories now under construction. Many experiments have measured some of these cross sections; however, no experiment had been undertaken which covered a wide range of target materials, production angles, and pion energies.¹⁻¹⁵ In the present work there was enough redundancy in the identification of particles so that counting efficiencies and backgrounds

could be accurately measured and taken into account in the computation of cross sections, and so that the proton and electron component in each momentum channel could also be measured. Here we report measurement of the differential cross section for pion production ($d^2\sigma/d\Omega dE$) by 730-MeV protons on H, D, Be, C, Al, Ti, Cu, Ag, Ta, Pb, and Th at eleven lab angles in the interval 15° – 150° and at twelve energies in the interval 25–550 MeV. The vast amount of data represented by this matrix of parameters required automatic data handling and reduction, which was accomplished using an on-line digital computer, with data reduction simultaneously done during the experiment. The experiment used the external proton beam of the

184-in. cyclotron at the Lawrence Radiation Laboratory, a liquid-hydrogen target and various solid targets, and a pion spectrometer consisting of a bending magnet and an array of 12 counter telescopes.

Some details of the earlier work follow: Forward pion cross sections for various nuclei were measured at 725 MeV by Haddock *et al.*¹ A group using 600-MeV protons from the CERN synchrocyclotron measured the pion spectra at 0.8° and 21.5° from hydrogen by a $\text{CH}_2\text{-C}$ difference, and also from various nuclei.²

Studies at 560, 600, and 970 MeV using liquid-hydrogen bubble chambers have been reported.³⁻⁵ Naturally the statistics were limited. In Ref. 3, for example, 233 events were identified of the class $p+p \rightarrow p+n+\pi^+$. A number of production experiments have been done by groups using the Dubna synchrocyclotron. Neganov and Savchenko⁶ measured the angular distributions for pions of energy >15 MeV for eight angles for proton energies from 480 to 660 MeV. Mescheriakov *et al.*⁷ measured the π^+ spectrum at 24° for the reaction $p+p \rightarrow p+n+\pi^+$, at 556 and 657 MeV. Meshkovskii *et al.* measured the same reaction for laboratory angles of 29° and 46° .⁸ Siderov,⁹ using emulsions, obtained the energy spectra of π^+ from 657-MeV protons on H at $\theta_{\text{lab}} = 60^\circ, 70^\circ, 90^\circ, 105^\circ, \text{ and } 120^\circ$. Batusov *et al.*,¹⁰ using emulsion chambers and 657-MeV protons, made similar measurements with somewhat differing results.

Production cross sections for 450-MeV protons on various nuclei at 21.5° and 60° have been measured by Lillethun.¹¹ Pion production from nuclei has been measured by workers at the Dubna synchrocyclotron and reported in a series of papers.¹²⁻¹⁵

An early review of production data from hydrogen was given by Gell-Mann and Watson.¹⁶ An interpretation of pion production data was given by Mandelstam¹⁷ in terms of a model based on the dominance of the $\Delta(1236)$ resonance. Lindenbaum and Sternheimer¹⁸ presented an isobar-model fit. At first glance, neither method looks very plausible for the pions of very low energy in the center-of-mass system. A model-independent approach was adopted by Schillaci, Silbar, and Young, who calculated pion production near threshold using the "soft-pion" technique.¹⁹ The resulting expression for the cross section, which has no adjustable parameters, gives values in fair agreement with measurements near threshold. This success encouraged them to extend the calculations to the production of low-energy *s*-wave pions at 740 MeV.²⁰ Other calculations were made by Drechsel and Weber.²¹ The results of such calculations are compared with the data in Sec. VI.

No adequate theory of the production in nuclei exists; however, cascade Monte Carlo calculations have been employed to represent the data,^{22,23} and some considerations have been given by Margolis.²⁴

In Sec. III we give details of the spectrometer, and in Sec. IV the details of the counters and the electronics. The data acquisition system, consisting of the PDP-8 computer, peripherals, interface, and software, is discussed in Sec. V. Details of the corrections to data are given in Appendixes. The results are discussed in Sec. VI.

II. EXPERIMENTAL ARRANGEMENT AND BEAM STUDIES

A. External Proton Beam, and Arrangement of Magnets and Shield

The experiment used the extracted proton beam; the beam viewed on a slow time scale was a pulse with a macro duty factor of $\sim 30\%$. The rf (52-nsec period) fine structure was 5%. Intensities of up to 70 nA could be obtained, but for data collection the beam current was reduced to keep dead time and multiple events to a low value; typically, 5–20 nA were used.

The beam line from the cyclotron through the physics cave is shown in Fig. 1. Starting from the cyclotron, the external beam passes through the PMC, which is a four-jaw adjustable collimator, a steering magnet (SM), a quadrupole doublet (Q_1Q_2), and then through a pipe in the shield and into the physics cave. In the cave are a quad doublet (CIRCE), the ion-chamber beam monitors, the target (T_1), and a split ion chamber (SIC); a second doublet quadrupole (DIANA) followed by a drift space. Finally, the beam stopped in a steel block ~ 10 m downstream from DIANA. The target position T_2 was used for backward production angles. When T_2 was in use, the SIC was relocated immediately downstream.

The quad pair Q_1Q_2 served to transport the beam to the cave; CIRCE was used to focus the beam at the target when it was at T_1 . DIANA served to transport the beam from T_1 to the beam stop, and, when the target was at T_2 , to focus the beam at T_2 .

The initial setup was for forward angles; the beam spot was adjusted using the Polaroid radiographs and a scintillating screen viewed by a TV system. The beam appeared to consist of two major components; these were separated horizontally at the location of the premagnet collimator (PMC) and focused on the target at different steering-magnet currents. A small spot of reasonable intensity was obtained at location T_1 by first setting the PMC to pass only one or the other of the com-

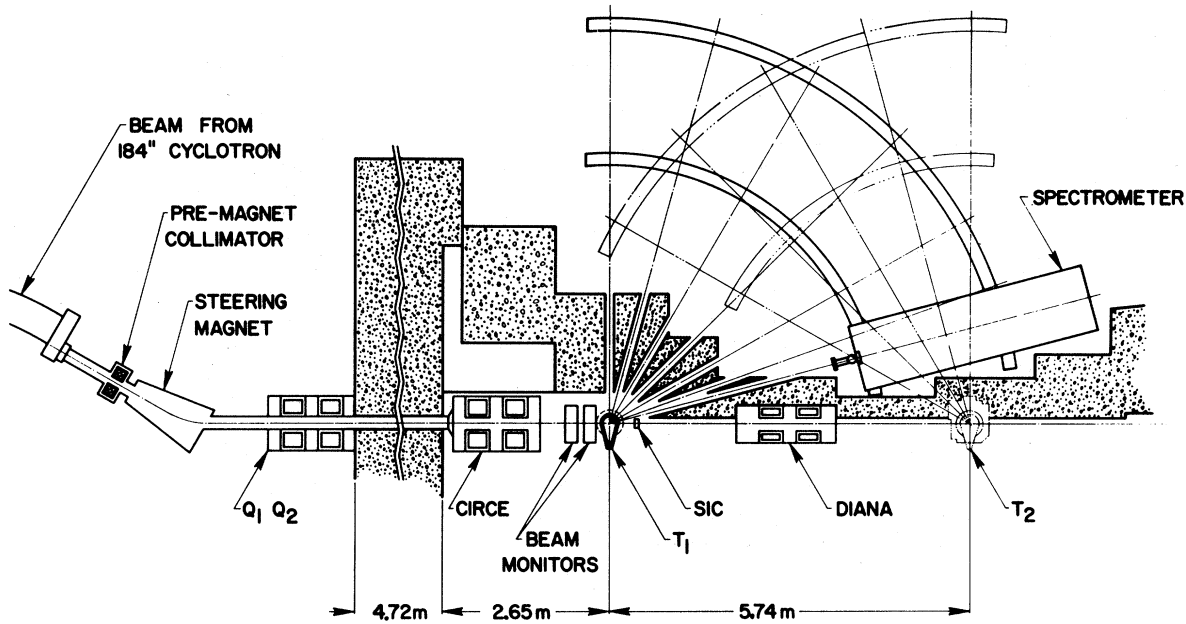


FIG. 1. Floor plan of beam line and spectrometer.

ponents, and then finding an appropriate setting for the quadrupoles. However, this procedure proved to be unsatisfactory; a significant part of the beam appeared as a low-current halo on one side, and was not all intercepted by the target. The PMC was then opened to include almost all of both beam components, and the quadrupoles were adjusted for as small a spot as possible. After the initial tests, the apparatus was set up for backward angles with the same PMC settings. The best spot obtainable at T_2 was perhaps too large for comfort with a 75-mm-diameter target, so 100-mm targets were used for most elements. After taking the backward-angle data, the setup was changed to forward angles, and the horizontal PMC was opened the rest of the way for these cross-section measurements.

B. Secondary Channels

Radiating out from the target positions were the secondary beam channels which the magnetic spectrometer viewed. These secondary channels from position T_1 were at angles of 15° , 20° , 30° , 45° , 60° , 75° , and 90° , with respect to the incident proton beam; at T_2 the channels were at 90° , 105° , 120° , 135° , and 150° . The channel opening was 10 cm horizontally by 12.5 cm vertically, or, when a lead collimator was inserted, 5 cm horizontally by 7.5 cm vertically. The lead collimator was inserted at a constant distance from the target so that scattering contributions at each angle were approximately the same. The collimator was used

to make an experimental determination of how many particles hit the walls of the channel and scattered back into the spectrometer. The collimator was removed for data taking, but a correction for the effect was applied to the data.

To correct for inscattering from the walls of the steel slot, the ratio of cross sections with the collimator in place and removed was measured, taking care that the target spot size was adequately small and that the collimator was aligned. This experimental test indicated that the collimator had essentially no effect on the highest momentum channels. However, the ratio of cross sections (collimator out vs collimator in) steadily increases with decreasing momentum to a value of 1.65 in the lowest momentum channel. The ratio was measured as a function of momentum, pion charge, target Z , and scattering angle, and was found to be quite insensitive to these variations; the ratios were therefore averaged. The averaged ratios are presented in Table I.

As a check, Monte Carlo calculations were made of the inscattering, including the effects of multiple Coulomb scattering, energy loss, and nuclear absorption in the channel walls. The calculation was done at energies of 50, 100, and 300 MeV for collimator out (smooth iron walls, 10 cm \times 12.5 cm \times 150 cm long) and collimator in (serrated lead walls, 5 cm \times 7.5 cm \times 125 cm long). The in-out ratio agreed fairly well with the measured numbers; the calculation showed there was an additional 15% inscattering even with the collimator in.

TABLE I. Channel parameters: Momentum, momentum width, and inscattering corrections and errors.

Channel	Central momentum (MeV/c)	Momentum width	Inscattering ratio ^a
0	674	31	0.93±0.14
1	606	30	0.95±0.12
2	526	29	0.99±0.11
3	474	27	1.02±0.10
4	419	26	1.07±0.10
5	365	24	1.10±0.09
6	311	22	1.17±0.09
7	255	20	1.23±0.10
8	195	17	1.33±0.11
9	161	15	1.40±0.11
10	123	13	1.49±0.13
11	81	8	1.65±0.26

^aRatio is cross section observed with collimator out compared to that observed with collimator in. Error is estimated uncertainty.

The inscattered particles were lower in energy by one channel or less.

The aperture of the spectrometer was defined by a scintillation counter mounted on the spectrometer, and not by the dimensions of the secondary beam channels. The spectrometer itself was mounted on rails, so that it could be moved to look at each of the secondary beam channels. There was a stray magnetic field from the cyclotron at the spectrometer; the vertical component varied between 5 and 10 G (downward) at different spectrometer locations and had the effect of displacing the pion beam transversely with respect to the spectrometer plane. Except for the very lowest momentum, this effect was very small.

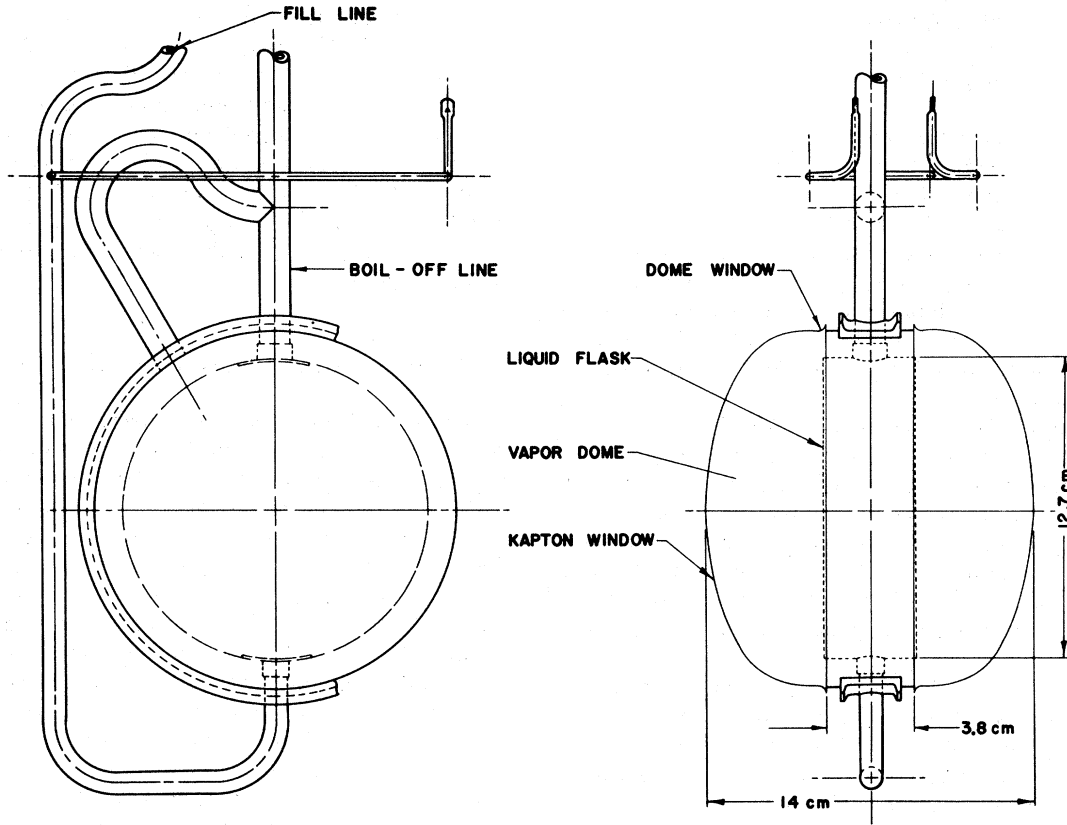
C. Beam Monitoring

1. Design

Four beam monitors were used during the experiment: (1) a counter telescope which viewed the particles produced by the interaction of the beam with a piece of Plexiglas; (2) a helium gas multi-gap ion chamber; (3) an argon-CO₂ gas ion chamber; and (4) several foils which were used for activation measurements. Of these only the counter telescope and helium ion chamber were available at all times during the experiment. The argon-CO₂ chamber and the foils were used occasionally as an absolute calibration of the telescope and helium chamber. The source of particles counted by the telescope was a piece of Plexiglas placed in the proton beam ~6 in. downstream from the snout. The ratio of counts in the monitor telescope to charge collected by the ion chamber changed by

<0.2% when the pion production targets were removed from the beam. Accidentals and pileup were measured and found to be negligible over the entire range of beam current available from the cyclotron. With a 12-mm Plexiglas source, the telescope-to-ion-chamber ratio was found to be insensitive to beam steering over a reasonable range of steering-magnet currents. However, we found that for the backward angle position of the production target, only 6 mm of Plexiglas could be tolerated because of the increase in beam size due to multiple scattering in the Plexiglas. In this case, the steering magnet caused a ±2% change in the telescope-to-ion-chamber ratio for a reasonable range of steering. During the data-taking period for forward angles, this ratio remained constant to better than ±0.4%, while for the backward-angle data, the ratio was constant to ±2%.

A helium ion chamber was located ~45 cm upstream of the production target. It was verified that the ratio of counts in the monitor telescope to charge collected from the ion chamber varied by 0.5% for a two-decade change in beam current. The calculated gain of this chamber was 165; however, an accident occurred during filling and we could not be sure that the gas was free of water vapor. Since the helium chamber operated reliably and its gain (relative to the monitor telescope) was stable over long periods of time, we chose to use this chamber as a relative monitor and to obtain an absolute calibration by comparison with an argon-CO₂ chamber and also by comparison with foil activation measurements. The gain value obtained was 183. Further details on ion chamber calibrations are given in Appendix A.

FIG. 2. H₂ cell.

D. Targets

1. Hydrogen Target

The target cell was designed to provide an unobscured angle of 270°. Figure 2 shows the front and side views of the hydrogen-target inner assembly. The liquid-hydrogen inner container (flask) is a 12.5-cm-diameter cylinder 4 cm deep, with windows of 18-mg/cm² Kapton. The flask is surrounded by a container (dome) for cold H₂ vapor in order to keep the pressure difference minimal across the flat windows; the window is 18-mg/cm² Kapton. The window of the vacuum jacket (not shown in Fig. 2) is also Kapton, of thickness 0.5 mm (70 mg/cm²). (The composition of Kapton is C₂₂H₁₀N₂O₅.) Counting rate differences between the flask full of liquid at pressure 760 mm and filled with vapor were taken. The equivalent number of protons is

$$N_p = 1.59 \times 10^{23} \text{ protons/cm}^2$$

The energy loss contributed by the target is computed for each pion channel.

2. Other Targets

Eleven different target materials were studied. The solid targets were either 7.5 cm or 10 cm in

diameter. A representative set of the materials and their respective areal densities is listed in Table II.

III. SPECTROMETER

A. Magnet Conversion and Measurement

The spectrometer magnet was constructed by modifying an existing LRL "C" magnet which had a 33-cm×61-cm pole face and a 15-cm gap. A yoke

TABLE II. Target densities.

Material	Areal density (g/cm ²)
LH ₂	^a
CD ₂	1.13
Be	0.90
C	1.10
Al	0.97
Ti	0.76
Cu	0.97
Ag	1.08
Ta	1.28
Pb	1.90
Th	1.01

^aSee Sec. C 1. Hydrogen target.

spacer was added to increase the gap. Triangular-shaped pole tips 15 cm thick were cut to provide a 61.5° wedge-shaped field with a 76-mm gap (Fig. 3).

The Z (normal) component of the field was measured in the median plane on a 13-mm \times 13-mm grid for all points where $B(x, y) \geq 10^{-4}B_0$, where B_0 , the central field, was chosen to be 11 kG. In addition, less detailed maps were made above and below the median plane to check for symmetry relative to the median plane. A median-plane map was also made, with $B_0 = 10$ kG, to allow the sensitivity of the focal properties to field variations to be determined.

The field values were checked for internal consistency via the OMNIBUS program written by the LRL magnetic measurements group. The field symmetry above and below the median plane was within 0.2% at locations of rapid spatial field variation (near the pole-tip edges) and within 0.01% in the high field region. The absolute error on each field measurement is believed to be smaller than 0.1% of B_0 .

Trajectories for the 12 momenta desired were traced using the median plane field map via an LRL code entitled FOCUS. The FOCUS program performs a numerical calculation of the trajectory of a charged particle of momentum p in the median plane of a dipole field, given a rectangular map of the magnetic field component normal to the plane of the particle orbit. In addition, the horizontal and vertical FOCUS matrices are calculated at each point along the trajectory. The magnetic field for any point (x, y) is calculated as needed by fitting the nearest three-by-three array of measured field values to a polynomial $B(x, y)$ which is of second degree in both x and y . The magnetic field and the needed space derivatives of the field are determined from the coefficients of $B(x, y)$. The central orbit paths and focal properties agreed surprising-

ly well with earlier calculations used for choosing the pole-tip wedge angle. These design calculations assumed that the magnetic field consisted of two triangular-shaped regions, one with field B_0 and one with the field reduced by the ratio of the gap spacings. The results of FOCUS allowed us to locate each of the twelve momentum-defining scintillation counters (S_3) at a focal point for the corresponding trajectory, and to center the other counters on the central orbits.

B. Spectrometer, Counter Mounting, and Alignment

The vertical aperture of the spectrometer was defined by counter S_0 located in front of the entrance to the magnet. The horizontal aperture was defined by counter S_1 located in front of the magnet (Fig. 3). Together they defined an acceptance aperture of 21.8×10^{-6} sr. Located between S_0 and S_1 was a methane-gas Čerenkov detector used to discriminate against electrons in the secondary beam. The third scintillation counter (S_2) was located against the sloping exit face of the magnet. The triple coincidence $S_0S_1S_2$ assured us that a charged particle had entered the spectrometer within its acceptance and had traversed the magnetic field. Twelve scintillation counters [$S_3(I)$], each 3.8 cm wide in the bending plane, were placed at the focal points of the desired trajectories to define the momentum band accepted by each channel. The telescope was completed by twelve larger scintillation counters [$S_4(I)$] placed behind the momentum-defining S_3 counters. In the six highest momentum channels, Plexiglas Čerenkov counters 2.5 cm thick were placed immediately behind the S_4 counters to aid in separating pions from protons.

The spectrometer carriage was made of steel I-beam, with counter mountings made of steel unistrut. All counters were surveyed in place. A

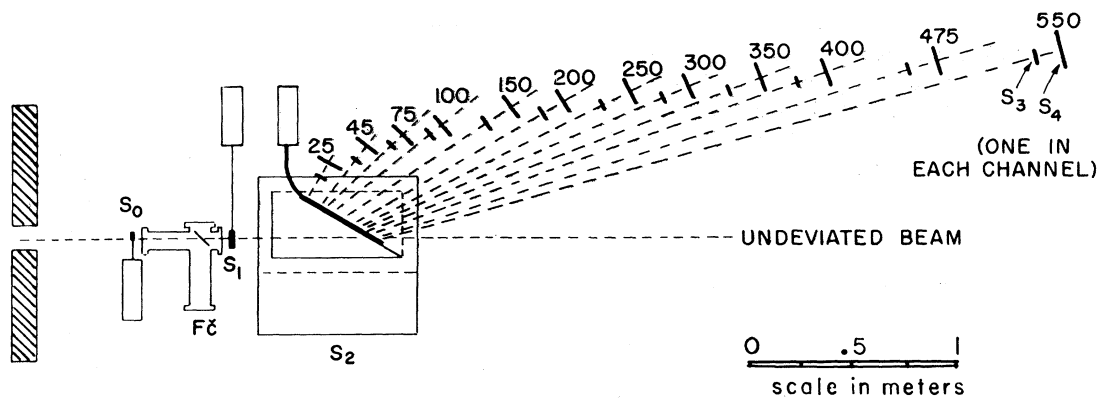


FIG. 3. Spectrometer.

with a 1.5- μ sec cycle time. This computer recorded events, monitored the spectrometer magnetic field, read the current integrators, logged information about each run, computed counter efficiencies, and classified events as pions, protons, electrons, or undecidable (zoo). During each run various computer-generated scope displays were available. At the end of each run the computer analyzed the data, computed cross sections, and printed and punched out the results.

B. Computer Interface

Figure 5 indicates the essential components of the interface between the fast counter electronics and the PDP-8. The devices to be interfaced fell into two main categories: (a) those which had to furnish data to the computer for every event, and (b) those which supplied data rarely, i.e., on request of the operator or at the end of a run. The former consisted of the momentum-channel information and the analog-to-digital converter data (time-of-flight and dE/dx information), and the latter of the real-time clock and the twelve 24-bit binary scalers which recorded various experimental parameters pertaining to an entire run rather than to single events.

C. Particle Identification and Displays

Pions were distinguished from protons in the same momentum channel by two criteria, time of flight and energy loss. Two time-to-amplitude converters were started by the signal from S_1 and stopped separately by S_3 and S_4 ; the average of these two times was compared with the limits for that channel to decide if the particle was a pion. Similarly, the energy loss in counters S_3 and S_4 was measured separately, and the geometric mean of the pulse heights was used.

As an aid to setting the limits, several histograms were available on the computer display scope. For each momentum channel there were two displays of the energy-loss spectrum, one for those events classified as pions by time of flight and one for those classified as protons; likewise, there were two time-of-flight spectra with classification by energy loss. The spectra observed contained few events above or below the expected peaks; the only critical limit was the one separating pions from protons.

Electrons were separated from pions by a Čerenkov counter; if the pulse height was sufficient, the event was tagged as an electron. The spectrum consisted of a broad peak, only partially separated from the noise. The pulse-height limit was set down in the noise to keep the percentage of electrons counted as pions down to less than 1%.

The error this introduced by tagging some pions as electrons was checked by the percentage of protons (by time of flight and energy loss) giving a Čerenkov pulse, and found to be small. Again no correction was applied.

D. On-Line Computer Programs

The program for the PDP-8 consisted of three major subsystems: (1) an executive program, (2) an event processor, and (3) an analysis program. The executive program handled the interrupts and performed all input-output operations. The event processor was called each time an event interrupt was detected, and performed all calculations which were required for each event. The analysis program was called once at the end of each run. The analysis program caused the fast scalers to be read into the computer, and then calculated efficiencies, calculated cross sections, and punched a paper tape record of the important data for each run.

The event processor performed three main tasks: (1) the preprocessing of data from the interface; (2) the sorting of events into logical classes; and (3) the collection of pulse-height distributions for diagnostic purposes.

The preprocessing was performed in three steps. First, the zoo bit and the momentum-channel bits from the interface were scanned, and all events with either a positive zoo bit or two or more momentum channels recorded simultaneously were rejected (such events would have confused the analog data system, making particle identification unreliable; hence they had to be rejected). The number of such events was tallied and no further processing was performed on them. For good events the functions

$$\frac{dE}{dx} = \left[\left(\frac{dE}{dx} \right)_{S_3(t)} \left(\frac{dE}{dx} \right)_{S_4(t)} \right]^{1/2}$$

and

$$\text{TOF} = \text{TOF1} + \text{TOF2}$$

were calculated. The use of the square root of the product of the two dE/dx signals rather than a single such signal had several advantages: (1) The particle identification was improved because of the reduction of the tail in the dE/dx product distribution; (2) the square root allowed a compression of scale (as compared with a product distribution) without any loss of information; and (3) the dependence of the gain of the scintillator on distance from the phototube was canceled (in first order) because the S_3 and S_4 phototubes were on opposite sides of the spectrometer midplane. Similarly, the computation of the sum of the two time-of-

TABLE III. Signals analyzed.

Name	Type	Possible logical result
Channel number	12-bit binary	Channel number 0-11
TOF (TOF1 + TOF2)	Analog	$\left\{ \begin{array}{l} 0 = \text{pion (or electron)} \\ 1 = \text{proton} \\ 2 = \text{bad data} \end{array} \right.$
$\frac{dE}{dx} = \left[\left(\frac{dE}{dx} \right)_{S_3(t)} \left(\frac{dE}{dx} \right)_{S_4(t)} \right]^{1/2}$	Analog	$\left\{ \begin{array}{l} 0 = \text{pion (or electron)} \\ 1 = \text{proton} \\ 2 = \text{bad data} \end{array} \right.$
LC	Analog	$\left\{ \begin{array}{l} 0 = \text{proton} \\ 1 = \text{proton (or electron)} \end{array} \right.$
FC	Analog	$\left\{ \begin{array}{l} 0 = \text{pion or proton} \\ 1 = \text{electron} \end{array} \right.$
ACC	Digital	$\left\{ \begin{array}{l} 0 = \text{good event} \\ 1 = \text{accidental event} \end{array} \right.$

flight signals improved the time resolution and canceled out the transit time differences in the S_3 and S_4 scintillators.

The event classification program first tested each of the analog signals against bias tables and determined a logical result. All of these bias tables were kept separately for each channel so that the best bias for each channel and each signal could be used without need for tedious gain-matching adjustments.

Two kinds of bias tests were used. The first was a single-bias test, in which the logical result was zero if the signal was less than or equal to the bias and one if it was greater than the bias. This test was used for the LC and FC signals. The second test was a four-bias test. A signal which fell between the first two biases was assigned a logical result of zero. A signal which fell between the third and fourth biases was assigned a logical result of one. All other events were given a logical result of two. This kind of test was used for both

the dE/dx and TOF signals. The complete list of signals used for event classification is given in Table III.

The pulse-height-analysis program collected 53 separate pulse-height distributions simultaneously. These one-dimensional spectra are shown in Table IV. Space was provided for only six LC spectra of each type, since these counters were installed only in the six channels which analyzed particles of the highest momenta. Because of the memory space limitations, only 32-channel pulse-height distributions were collected for the first 50 spectra tabulated. The last three, namely FC_e , $FC_{\bar{e}}$, and a spare, were 256-channel spectra. The spare was provided so that any single spectrum could be examined in finer detail if desired.

At the end of each run, the analysis program was initiated. First, the computer read the fast scalers and constructed several ratios useful for consistency checks of the experiment. In addition, the range setting of the helium-ion-chamber cur-

TABLE IV. Types of pulse-height spectra stored on line.

Signal source	Event type	Momentum channels
TOF	Pion	Kept separately for all 12 channels
	Proton	Kept separately for all 12 channels
$\frac{dE}{dx}$	Pion	Kept separately for all 12 channels
	Proton	Kept separately for all 12 channels
LC	Pion	Six momentum channels
	Proton	Six momentum channels
FC	Electron	All 12 channels summed
	Pion or proton	All 12 channels summed
Spare (any)	Any	Any one channel or all 12 channels summed

rent integrator was read. From this information and the integrator counts recorded in the scalers, the number of protons passing through the target was computed.

The next step in the analysis was to determine the number of pions, protons, and electrons counted in each momentum channel. For example, the program classified events in a given momentum channel as pions if the time-of-flight and the dE/dx signals were within the established windows, and if the gas Čerenkov counter gave no signal.

The PDP-8 memory contained typed-in data for each run about target, angle setting, etc., permanent tables of $\Delta\Omega\Delta E$ for each momentum channel, precalculated tables of channel momentum, a matrix to make the $\pi\mu$ decay correction, and a table of target atoms/cm². With this information and with the data corrected during the run, the program computed preliminary values of the production cross sections, corrected for computer dead time, zoo (unclassified) events, and $\pi\mu$ decay. The PDP-8 typed out these cross sections and punched out the data on paper tape.

E. Off-Line Data Reduction

The paper tape output was transcribed to magnetic tape and to cards for further processing at Los Alamos on the CDC-6600 computer. There, additional corrections were made to the data.

The most important of these corrections was that for the effects of inscattering discussed in Sec. II. In the final data reduction the inscattering corrections (Table I) were applied to the measured pion and proton cross sections on a channel-by-channel basis, independent of the spectrum. The errors on the inscattering correction were estimated by comparing the experimental ratio results with each other and with the Monte Carlo results. Before the inscattering corrections were applied, the c.m. angular distributions for hydrogen, which should have forward-backward symmetry, were asymmetric. After applying the correction, the angular distributions became essentially symmetric.

Additional corrections were made for pion absorption in the production target (small) and for pion energy loss in the materials before momen-

TABLE V. Ratio of E^+ to π^+ from Cu.

Angle (deg)	Electron energy (MeV)											
	98	132	168	201	259	315	369	423	478	530	610	678
15	0.807 ±0.071	0.234 ±0.018	0.121 ±0.012	0.066 ±0.007	0.026 ±0.004	0.014 ±0.002	0.005 ±0.001	0.004 ±0.001	0.003 ±0.001	0.001 ±0.001	0.005 ±0.003	
20	0.528 ±0.044	0.138 ±0.011	0.082 ±0.007	0.039 ±0.005	0.020 ±0.003	0.010 ±0.002	0.003 ±0.001					
30	0.489 ±0.032	0.128 ±0.009	0.063 ±0.005	0.040 ±0.004	0.018 ±0.002	0.009 ±0.001	0.003 ±0.001	0.002 ±0.001	0.002 ±0.001	0.003 ±0.002		
45	0.280 ±0.018	0.082 ±0.006	0.040 ±0.003	0.024 ±0.002	0.007 ±0.001	0.003 ±0.001	0.003 ±0.001					
60	0.147 ±0.011	0.040 ±0.003	0.021 ±0.002	0.012 ±0.002	0.004 ±0.001	0.003 ±0.001	0.002 ±0.001	0.002 ±0.002				
75	0.115 ±0.007	0.035 ±0.002	0.016 ±0.002	0.007 ±0.001	0.004 ±0.001	0.004 ±0.001	0.001 ±0.001	0.011 ±0.006	0.010 ±0.010	0.044 ±0.044		
90	0.149 ±0.006	0.034 ±0.002	0.012 ±0.001	0.007 ±0.001	0.003 ±0.001							
105	0.112 ±0.006	0.022 ±0.002	0.008 ±0.001	0.005 ±0.001	0.002 ±0.001	0.003 ±0.002						
120	0.079 ±0.005	0.018 ±0.002	0.007 ±0.001	0.003 ±0.001								
135	0.062 ±0.004	0.017 ±0.001	0.006 ±0.001	0.003 ±0.001								
150	0.075 ±0.005	0.016 ±0.002	0.004 ±0.001	0.005 ±0.001	0.003 ±0.002							

TABLE VI. Ratio of E^- to π^- from Cu.

Angle (deg)	Electron energy (MeV)											
	98	132	168	201	259	315	369	423	478	530	610	678
15	0.760 ± 0.034	0.414 ± 0.016	0.245 ± 0.012	0.155 ± 0.009	0.082 ± 0.006	0.051 ± 0.005	0.021 ± 0.003	0.014 ± 0.003	0.009 ± 0.003	0.006 ± 0.006		
20	0.668 ± 0.023	0.318 ± 0.011	0.205 ± 0.009	0.130 ± 0.006	0.074 ± 0.004	0.042 ± 0.003	0.027 ± 0.003	0.015 ± 0.002	0.009 ± 0.002	0.009 ± 0.004	0.013 ± 0.009	
30	0.584 ± 0.019	0.278 ± 0.009	0.166 ± 0.007	0.109 ± 0.005	0.051 ± 0.004	0.029 ± 0.003	0.015 ± 0.002	0.007 ± 0.002	0.004 ± 0.002			
45	0.425 ± 0.016	0.190 ± 0.008	0.119 ± 0.006	0.068 ± 0.004	0.030 ± 0.003	0.023 ± 0.003	0.014 ± 0.003	0.011 ± 0.004	0.011 ± 0.005			
60	0.305 ± 0.010	0.119 ± 0.005	0.069 ± 0.004	0.038 ± 0.003	0.018 ± 0.002	0.010 ± 0.002	0.012 ± 0.004	0.016 ± 0.007				
75	0.280 ± 0.010	0.106 ± 0.005	0.054 ± 0.004	0.032 ± 0.003	0.019 ± 0.003	0.015 ± 0.004	0.018 ± 0.008					
90	0.303 ± 0.009	0.108 ± 0.004	0.059 ± 0.003	0.033 ± 0.003	0.018 ± 0.003	0.009 ± 0.004						
105	0.247 ± 0.009	0.078 ± 0.004	0.039 ± 0.003	0.018 ± 0.003	0.002 ± 0.003	0.008 ± 0.006						
120	0.169 ± 0.006	0.064 ± 0.003	0.034 ± 0.003	0.019 ± 0.003	0.005 ± 0.003							
135	0.167 ± 0.007	0.053 ± 0.003	0.030 ± 0.003	0.010 ± 0.002	0.015 ± 0.006	0.024 ± 0.017						
150	0.138 ± 0.006	0.051 ± 0.003	0.029 ± 0.003	0.014 ± 0.003	0.003 ± 0.003							

tum analysis. Some minor modifications were made to the on-line $\pi\mu$ decay correction.

The effects of multiple Coulomb scattering in causing loss of particles were calculated. The correction was negligible and none was applied.

VI. RESULTS

The corrected cross sections are presented in the form of tables and curves. Energies and angles refer to the laboratory system. Errors listed include both statistical errors and uncertainties arising from the various calibrations and corrections. Pion differential cross sections are given for the following target materials: H, D, Be, C, Al, Cu, and Pb. Data for the other target nuclei will be published elsewhere.

The pion cross sections and their errors are discussed in Secs. IV and V. Summarizing these discussions, we can say that the systematic error in the beam-current measurement (which affects all cross sections the same) introduced by the uncertainty in our calibration of ion-chamber gain is believed to be about 10%. This is not included in the stated errors. The channel-inscattering correction introduces an average uncertainty of 10%,

and is included in the stated errors. The other corrections and estimates introduce relatively small uncertainty, which is included in the stated errors, namely the estimates of solid angle, momentum interval, target number, counter efficiency, corrections for $\pi\mu$ decay, target absorption, computer deadtime, zoo events, etc. The statistical uncertainty is typically of the order of 3%.

The protons are believed to come from scattering and from nuclear reactions in the target, and the appropriate corrections have been applied to them. The tabulated proton cross sections should provide a reliable guide for calculating beam contamination in experimental setups. The positrons and electrons arise from π and μ decay in flight and from π^0 γ decay and subsequent pair production in the general region of the target. There may be some contribution from reactions in the channel wall. The electron numbers should be regarded only as an order-of-magnitude indication of the backgrounds to be encountered in an experimental setup, and are presented as the ratio of e^+/π^+ ; the number of e^+ is approximately equal to the number of e^- . Results are given here for electrons and protons from the copper target only (Tables V–VII). More extensive tables of protons and electron data will be published elsewhere.

TABLE VII. Cross section for p from Cu in $\mu\text{b sr}^{-1}\text{MeV}^{-1}$.

Angle (deg)	Proton energy (MeV)							
	60	71	86	103	125	148	188	225
15	306.2 ± 35.2	630.5 ± 66.3	592.3 ± 57.3	629.2 ± 69.4	680.6 ± 78.7	677.0 ± 88.7	659.9 ± 98.2	625.9 ± 111.0
20	354.6 ± 40.5	622.4 ± 65.3	559.6 ± 54.1	583.0 ± 64.3	600.3 ± 69.4	595.7 ± 78.0	568.3 ± 84.6	522.3 ± 92.6
30	369.9 ± 42.1	636.5 ± 66.6	566.5 ± 54.7	580.0 ± 63.9	588.9 ± 68.0	568.2 ± 74.4	505.2 ± 75.2	444.4 ± 78.8
45	344.0 ± 39.1	550.7 ± 57.6	478.0 ± 46.1	478.2 ± 52.7	475.3 ± 54.9	449.0 ± 58.7	391.3 ± 58.2	338.1 ± 59.9
60	334.2 ± 37.9	513.2 ± 53.7	431.2 ± 41.6	415.0 ± 45.7	398.8 ± 46.1	364.1 ± 47.6	282.7 ± 42.0	203.7 ± 36.1
75	286.5 ± 32.5	408.0 ± 42.7	335.0 ± 32.3	297.3 ± 32.7	256.1 ± 29.6	204.6 ± 26.8	125.8 ± 18.7	75.1 ± 13.3
90	214.5 ± 24.3	264.9 ± 27.7	200.6 ± 19.3	164.3 ± 18.1	129.9 ± 15.0	92.2 ± 12.1	49.1 ± 7.3	23.6 ± 4.2
105	196.6 ± 22.3	204.1 ± 21.4	150.3 ± 14.5	112.3 ± 12.4	80.7 ± 9.3	53.3 ± 7.0	23.0 ± 3.4	8.8 ± 1.6
120	86.5 ± 9.9	122.8 ± 12.9	84.9 ± 8.2	66.0 ± 7.3	45.4 ± 5.3	28.0 ± 3.7	10.2 ± 1.5	3.4 ± 0.6
135	66.2 ± 7.5	90.1 ± 9.4	65.6 ± 6.4	49.9 ± 5.5	34.2 ± 4.0	19.3 ± 2.5	6.1 ± 0.9	1.6 ± 0.3
150	60.7 ± 6.9	82.3 ± 8.7	53.9 ± 5.2	42.4 ± 4.7	28.3 ± 3.3	15.5 ± 2.1	4.6 ± 0.7	1.2 ± 0.2

A. π Production in Hydrogen

Several qualitative features may be seen in the hydrogen data, (Fig. 6, Tables VIII, IX). First, π^- from liquid hydrogen (LH) are observed at energies up to 250 MeV, and at angles of 15° , 20° , and 30° , but predominantly at 15° and the lowest energies (30 and 52 MeV). The cross section is only a few percent of that for positive pions. π^- mesons come from the reaction $p+p \rightarrow \pi^+ + \pi^- + p$. We can interpret the π^- peaking near zero energy and angles as the influence of the Δ^{++} resonance, according to the one-pion-exchange (OPE) diagram (Fig. 7). The Δ^{++} tends to be formed

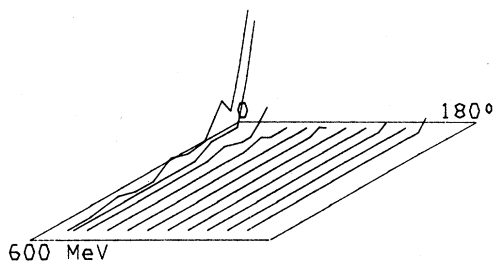


FIG. 6. Cross section for π^- production from liquid hydrogen. The solid lines are polygons with the data points as vertices.

near the resonance energy, in effect reducing the amount of energy available for the $n \rightarrow p + \pi^-$ branch.

The curve for π^+ production (Fig. 8) shows a very strong forward peaking at all energies, the maximum cross section being at 15° and 305 MeV. This behavior is to be expected on an isobar model,^{16,17} where the $\Delta(1236)$ formation and decay dominates the production process. Partly phenomenological treatments, assuming that Δ formation dominates the pion-nucleon interaction at these energies, have been reasonably successful.¹⁶⁻¹⁸ More recently a number of calculations have been made on the basis of the peripheral or one-pion-

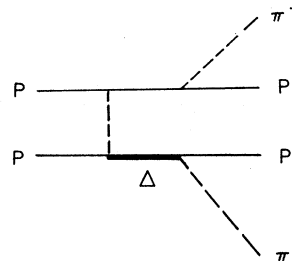


FIG. 7. One-pion-exchange diagram of $\pi^+ \pi^-$ production from hydrogen. The Δ^{++} tends to be formed near the resonance energy, leaving little energy for the π^- .

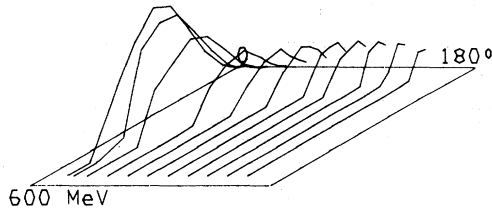


FIG. 8. Cross section for π^+ production from liquid hydrogen. The solid lines are polygons with the experimental data points as vertices.

fairly good except for the lowest-energy and the highest-energy pions. The highest-energy pions come from the reaction $p + p \rightarrow \pi^+ + d$, which is not included in their calculated curves.²⁶ Two of us have recently participated in a measurement of $p + p \rightarrow \pi^+ + d$ at higher proton momenta (3.4–12.3 GeV/c).²⁹ The behavior of the cross section below 4-GeV/c proton momentum can also be interpreted in terms of the OPE model, with a final-state interaction between the two nucleons.³⁰

As for the low-energy pions, attempts have been made to calculate the cross section for low-energy pions using the soft-pion approximation.¹⁹ At proton energies near threshold, the method had some success, but at the present energy the soft-pion contribution is small compared to the total.²⁰ We find experimentally for the low-energy pion cross section

$$\frac{d^2\sigma}{d\Omega dp} \cong 10^{-4} p^2 [1.2 \pm 0.13 + (0.22 \pm 0.4) \cos^2 \theta],$$

where p and θ are respectively the pion momentum and angle in the center-of-mass system. This value, while not in disagreement with CERN² and Berkeley¹ data, is about eight times higher than the soft-pion prediction. As Schillaci and Silbar point out,³¹ the Δ isobar, which was not included in their calculation,¹⁹ is also responsible for the large low-energy pion emission. Extending the Mandelstam model¹⁷ to this energy gives qualitative agreement. Essentially pions emitted from the Δ decaying backward can appear in the laboratory system as copious low-energy pions.

Drechsel and Weber²¹ are able to account for the full spectra by evaluating diagrams for one-boson exchange (OBE) and one-pion exchange (OPE). The OBE contributes a nucleon-pole term to the production amplitude and appears to enhance especially the low-energy pions. In summary, it appears that peripheral processes are dominant in the π production at this energy.

B. Deuterium

The deuterium data (Tables X, XI) are the result of a CD_2 -D subtraction. In the π^-D data, Table XI, we see a sharp rise in σ near 0° and low energy, suggesting that the same pion-pair mechanism is operating as in H. We also see a broader spectrum superimposed from the reaction $p + n$

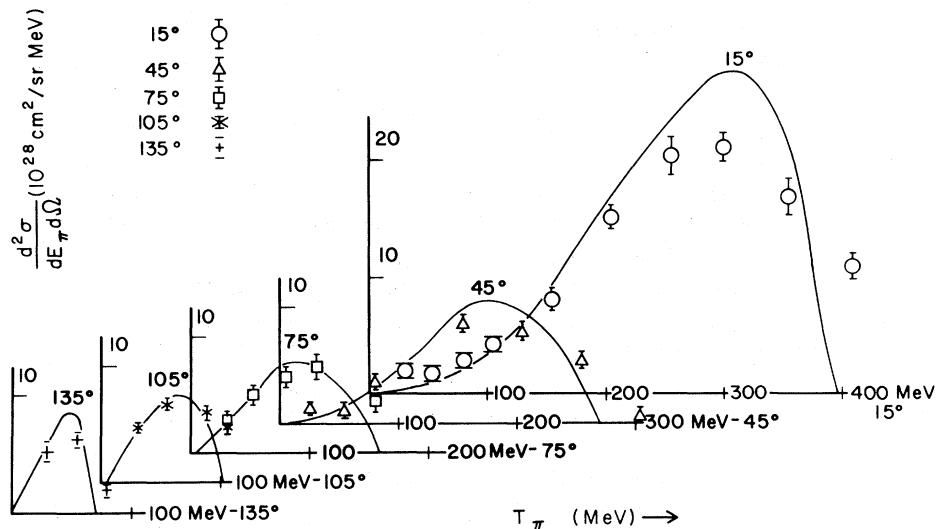


FIG. 9. π^+ spectra from liquid hydrogen. Solid curves, calculated by Suslenko and Kochkin, are the OPE model for the reaction $p + p \rightarrow n + p + \pi^+$. The reaction $p + p \rightarrow d + \pi^+$ is not included in their calculations.

TABLE X. Cross section for π^+ from D in $\mu\text{b sr}^{-1}\text{MeV}^{-1}$.

Angle (deg)	Pion energy (MeV)											
	30	52	79	105	155	205	255	305	358	408	486	553
15	2.67 ± 0.80	2.29 ± 0.49	3.33 ± 0.56	5.90 ± 0.74	8.73 ± 0.92	12.18 ± 1.11	16.24 ± 1.48	18.46 ± 1.83	16.37 ± 1.69	5.92 ± 0.74	0.37 ± 0.15	0.11 ± 0.07
20	1.71 ± 0.60	1.50 ± 0.40	3.15 ± 0.49	4.05 ± 0.57	7.23 ± 0.76	11.78 ± 1.04	14.16 ± 1.27	14.42 ± 1.43	12.78 ± 1.32	3.10 ± 0.42		
30	2.47 ± 0.60	2.22 ± 0.38	2.44 ± 0.39	3.49 ± 0.48	8.13 ± 0.76	10.79 ± 0.91	11.81 ± 1.04	9.83 ± 0.97	5.00 ± 0.54	0.26 ± 0.11	0.08 ± 0.05	
45	1.74 ± 0.38	2.48 ± 0.30	3.26 ± 0.33	5.00 ± 0.47	6.95 ± 0.60	6.27 ± 0.52	4.35 ± 0.39	1.05 ± 0.13	0.24 ± 0.06			
60	2.46 ± 0.44	3.44 ± 0.34	5.18 ± 0.44	6.40 ± 0.55	5.21 ± 0.44	2.57 ± 0.21	0.57 ± 0.06	0.14 ± 0.03	0.05 ± 0.02			
75	4.90 ± 0.83	6.97 ± 0.65	8.47 ± 0.70	8.38 ± 0.72	4.54 ± 0.39	1.16 ± 0.11	0.21 ± 0.04	0.08 ± 0.02				
90	7.78 ± 1.25	11.58 ± 1.02	10.91 ± 0.87	8.90 ± 0.74	2.23 ± 0.19	0.45 ± 0.04	0.11 ± 0.01	0.02 ± 0.01				

$\rightarrow \pi^- + 2p$. The cross section $\sigma_D(\pi^+)$, Table IX, is significantly less than $\sigma_H(\pi^+) + \sigma_H(\pi^-)$, indeed less than $\sigma_H(\pi^+)$ alone. There is either a strong interference or a Glauber-type shadowing. The $+/-$ ratio (Table XII) is 10.2 ± 0.8 , where an isobar model would predict 11.

C. Beryllium

The Be cross-section data are given in Tables XIII and XIV. The $\text{Be}(\pi^+)$ cross section is about

double the $\text{H}(\pi^+)$ value. No remarkable structure is evident in the spectrum or the angular distribution. The forward low-energy peak for π^- seen in the hydrogen isotopes has disappeared.

D. Carbon

The C cross-section data are given in Tables XV and XVI. The total cross section for carbon is about $2.7\sigma_H$. The π^+ doubly differential spectrum has a broad maximum at about 250 MeV and is

TABLE XI. Cross section for π^- from D in $\mu\text{b sr}^{-1}\text{MeV}^{-1}$.

Angle (deg)	Pion energy (MeV)											
	30	52	79	105	155	205	255	305	358	408	486	553
15	1.24 ± 0.24	0.79 ± 0.11	0.77 ± 0.10	0.79 ± 0.11	1.35 ± 0.13	1.74 ± 0.16	2.23 ± 0.20	1.91 ± 0.19	1.12 ± 0.12	0.10 ± 0.03		
20	1.24 ± 0.23	0.65 ± 0.10	0.80 ± 0.10	0.85 ± 0.11	1.16 ± 0.12	1.50 ± 0.13	1.82 ± 0.16	1.43 ± 0.14	0.64 ± 0.07			
30	0.26 ± 0.12	0.40 ± 0.09	0.48 ± 0.09	0.69 ± 0.10	1.05 ± 0.11	1.30 ± 0.12	1.33 ± 0.13	0.70 ± 0.08	0.17 ± 0.03			
45	0.35 ± 0.07	0.40 ± 0.05	0.50 ± 0.05	0.76 ± 0.07	1.04 ± 0.09	0.82 ± 0.07	0.31 ± 0.03	0.04 ± 0.01				
60	0.48 ± 0.08	0.54 ± 0.05	0.71 ± 0.06	0.92 ± 0.08	0.68 ± 0.06	0.23 ± 0.02	0.04 ± 0.01					
75	0.33 ± 0.07	0.42 ± 0.05	0.56 ± 0.05	0.59 ± 0.05	0.20 ± 0.02	0.03 ± 0.01						
90	0.41 ± 0.08	0.49 ± 0.06	0.43 ± 0.04	0.29 ± 0.03	0.03 ± 0.01							

TABLE XII. Total cross sections for π^+ and π^- .

Element	σ^+	σ^-	Ratio
H	13.50±0.73	0.03±0.01	45
D	11.42±0.55	1.12±0.06	10.2
Be	27.30±1.40	6.49±0.37	4.3
C	35.00±1.80	6.64±0.41	5.3
Al	53.10±2.90	13.17±0.90	4.0
Ti	67.00±3.60	21.20±1.60	3.2
Cu	77.30±4.30	25.20±2.0	3.1
Ag	91.60±5.10	35.00±3.0	2.6
Ta	101.00±5.60	51.40±4.70	2.0
Pb	104.20±5.80	53.70±4.90	1.95
Th	107.90±5.90	60.40±5.50	1.9

strongly forward (Fig. 10). The π^- spectrum, Fig. 11, is also strongly forward, but shifted to lower energies, the maximum being at 50 MeV. The +/- ratio is 5.4, compared to the isobar-model prediction.²⁴ The shape of the pion spectra can be accounted for by a Monte Carlo calculation of an internucleon cascade process,^{22,23} in which the initial production of a pion is via a free nucleon-nucleon

process, with experimental production spectra used,^{3-8,12,14} and with the pion subsequently followed through the remainder of the nucleus. Rescattering, energy degradation, and absorption are taken into account. A limitation of this method is the substantial amount of computer time required per pion traced, which is reflected in the small number of pions traced, and the consequent statistical fluctuations in the output. Figures 12 and 13 show some of the carbon data compared with the Monte Carlo calculations.³²

E. Heavier Elements

Cross-section data for Al, Cu, and Pb are given in Tables XVII-XXII. In Table XII we list total cross sections, namely, $\sigma_T \equiv \int (d^2\sigma/d\Omega dE)d\Omega dE$, and the ratios of π^+ to π^- production. [Note that the +/- ratio drops from 45 in hydrogen to 1.9 in thorium.] Figure 14 shows $\sigma_T(\pi^+)/Z^{1/3}$ vs Z . Beyond carbon we have, to a good approximation,

$$\sigma_T^+ \approx 24.5 Z^{1/3}.$$

On the other hand, for π^- (Fig. 15), σ_T is proportional to $N^{2/3}$ beyond carbon:

TABLE XIII. Cross section for π^+ from Be in $\mu\text{b sr}^{-1}\text{MeV}^{-1}$.

Angle (deg)	Pion energy (MeV)											
	30	52	79	105	155	205	255	305	358	408	486	553
15	5.23 ± 0.86	6.57 ± 0.60	10.30 ± 0.84	15.66 ± 1.32	22.80 ± 1.87	27.97 ± 2.17	33.10 ± 2.72	32.95 ± 3.09	23.94 ± 2.36	10.91 ± 1.22	2.21 ± 0.29	0.35 ± 0.06
20	5.14 ± 0.88	6.54 ± 0.62	10.00 ± 0.83	14.68 ± 1.25	20.52 ± 1.70	23.61 ± 1.84	27.66 ± 2.29	25.67 ± 2.42	17.36 ± 1.72	6.62 ± 0.75	1.28 ± 0.18	0.12 ± 0.03
30	4.94 ± 0.83	7.05 ± 0.66	10.52 ± 0.87	14.54 ± 1.23	19.67 ± 1.62	22.11 ± 1.73	21.25 ± 1.76	15.04 ± 1.43	7.69 ± 0.77	2.69 ± 0.31	0.35 ± 0.06	0.04 ± 0.01
45	4.96 ± 0.83	7.34 ± 0.67	9.94 ± 0.81	13.77 ± 1.16	14.57 ± 1.20	11.76 ± 0.93	7.73 ± 0.65	3.38 ± 0.33	1.26 ± 0.14	0.26 ± 0.04	0.03 ± 0.01	
60	6.20 ± 1.00	9.60 ± 0.86	11.54 ± 0.92	13.75 ± 1.15	9.29 ± 0.77	5.11 ± 0.40	2.13 ± 0.18	0.70 ± 0.07	0.25 ± 0.03	0.03 ± 0.01		
75	8.04 ± 1.29	12.03 ± 1.06	13.15 ± 1.05	12.66 ± 1.06	5.96 ± 0.49	2.12 ± 0.17	0.60 ± 0.06	0.21 ± 0.03	0.04 ± 0.01			
90	9.59 ± 1.51	13.54 ± 1.18	12.41 ± 0.98	9.83 ± 0.82	3.08 ± 0.25	0.80 ± 0.06	0.19 ± 0.01	0.05 ± 0.01				
105	11.12 ± 1.76	15.16 ± 1.33	12.27 ± 0.97	7.53 ± 0.63	1.72 ± 0.15	0.36 ± 0.03	0.07 ± 0.01					
120	9.67 ± 1.54	12.27 ± 1.08	8.70 ± 0.69	4.69 ± 0.39	0.88 ± 0.08	0.17 ± 0.02	0.03 ± 0.01					
135	8.21 ± 1.30	10.63 ± 0.93	6.70 ± 0.53	3.41 ± 0.28	0.54 ± 0.04	0.08 ± 0.01						
150	7.65 ± 1.21	9.15 ± 0.80	5.44 ± 0.43	2.69 ± 0.23	0.40 ± 0.03	0.06 ± 0.01						

TABLE XIV. Cross section for π^- from Be in $\mu\text{bsr}^{-1}\text{MeV}^{-1}$.

Angle (deg)	Pion energy (MeV)											
	30	52	79	105	155	205	255	305	358	408	486	553
15	2.81 ± 0.47	2.92 ± 0.27	3.60 ± 0.30	4.49 ± 0.38	5.13 ± 0.43	5.28 ± 0.42	5.52 ± 0.46	4.43 ± 0.42	2.68 ± 0.27	0.72 ± 0.09	0.15 ± 0.03	0.03 ± 0.01
20	2.74 ± 0.45	2.88 ± 0.26	3.24 ± 0.27	4.12 ± 0.35	4.69 ± 0.39	4.81 ± 0.38	4.62 ± 0.39	3.66 ± 0.35	1.98 ± 0.20	0.59 ± 0.07	0.11 ± 0.02	0.02 ± 0.01
30	2.09 ± 0.35	2.43 ± 0.23	3.25 ± 0.27	4.46 ± 0.38	4.53 ± 0.38	4.38 ± 0.35	3.72 ± 0.31	2.25 ± 0.22	0.98 ± 0.10	0.25 ± 0.03	0.03 ± 0.01	
45	1.76 ± 0.28	2.43 ± 0.22	2.89 ± 0.23	3.71 ± 0.31	3.33 ± 0.28	2.56 ± 0.20	1.44 ± 0.12	0.58 ± 0.06	0.18 ± 0.02	0.03 ± 0.01		
60	2.14 ± 0.34	2.76 ± 0.25	3.15 ± 0.25	3.44 ± 0.29	2.30 ± 0.19	1.08 ± 0.09	0.40 ± 0.04	0.13 ± 0.01	0.03 ± 0.01			
75	2.47 ± 0.40	3.36 ± 0.30	3.37 ± 0.27	2.96 ± 0.25	1.27 ± 0.11	0.44 ± 0.04	0.12 ± 0.01	0.03 ± 0.01				
90	3.06 ± 0.49	3.64 ± 0.32	3.18 ± 0.25	2.32 ± 0.19	0.74 ± 0.06	0.20 ± 0.02	0.04 ± 0.01					
105	3.44 ± 0.55	3.65 ± 0.32	2.77 ± 0.22	1.74 ± 0.14	0.44 ± 0.04	0.09 ± 0.01						
120	2.78 ± 0.44	3.09 ± 0.27	2.13 ± 0.17	1.18 ± 0.10	0.25 ± 0.02	0.04 ± 0.01						
135	2.30 ± 0.37	3.00 ± 0.26	1.91 ± 0.15	1.02 ± 0.09	0.19 ± 0.02	0.03 ± 0.01						
150	1.81 ± 0.29	2.29 ± 0.20	1.47 ± 0.12	0.76 ± 0.06	0.12 ± 0.01	0.02 ± 0.01						

$$\sigma_{\pi^-} = 2.33N^{2/3}.$$

Figures 16 and 17 show some experimental results and the cascade Monte Carlo calculations for Cu. Noteworthy are the large numbers of low-energy π^- at 90° . The agreement is comparable for all the other elements. Figures 18 and 19 show the complete experimental distributions from copper, and Figs. 20 and 21 those from thorium. The striking feature of these curves is the buildup of negative pions in the heavier elements. Negative pions are relatively more copious than in hydrogen, are predominantly of low energy, and are

emitted over a wide range of angles. In contrast, the positive pions are predominantly at forward angles, and the spectrum peaks at about 250 MeV. The shape of the spectra and angular distribution is rather constant from one nucleus to the next from Cu to Th for either sign of pion. Indeed the following approximate scaling law holds for elements from Al to Th:

$$\frac{d^2\sigma(A)}{d\Omega dE} / \sigma_T(A) = \frac{d^2\sigma(B)}{d\Omega dE} / \sigma_T(B).$$

Figures 22 to 25 show the degree of validity of the

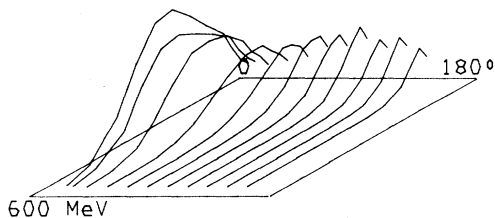


FIG. 10. Cross section for π^+ from C. Solid lines are polygons through the data points.

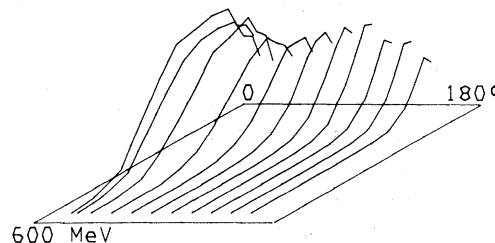


FIG. 11. Cross section for π^- from C.

TABLE XV. Cross section for π^+ from C in $\mu\text{b}\text{sr}^{-1}\text{MeV}^{-1}$.

Angle (deg)	Pion energy (MeV)											
	30	52	79	105	155	205	255	305	358	408	486	553
15	6.93 ± 1.25	9.19 ± 0.92	14.93 ± 1.28	21.36 ± 1.86	27.15 ± 2.29	33.53 ± 2.65	38.77 ± 3.23	37.60 ± 3.56	27.17 ± 2.70	13.73 ± 1.56	3.18 ± 0.43	0.46 ± 0.10
20	7.34 ± 1.25	10.05 ± 0.95	14.36 ± 1.19	20.34 ± 1.73	24.23 ± 2.01	27.63 ± 2.17	30.54 ± 2.54	29.04 ± 2.74	20.57 ± 2.04	8.67 ± 0.99	2.06 ± 0.28	0.28 ± 0.06
30	6.37 ± 1.09	10.35 ± 0.97	13.84 ± 1.15	18.87 ± 1.61	24.05 ± 1.99	25.26 ± 1.98	24.62 ± 2.05	18.18 ± 1.73	9.57 ± 0.96	3.55 ± 0.42	0.50 ± 0.08	0.06 ± 0.02
45	7.69 ± 1.26	11.14 ± 1.00	14.08 ± 1.14	17.54 ± 1.48	17.39 ± 1.43	13.92 ± 1.09	9.04 ± 0.76	4.45 ± 0.43	1.80 ± 0.19	0.43 ± 0.06	0.04 ± 0.01	0.02 ± 0.01
60	9.05 ± 1.46	13.79 ± 1.23	15.96 ± 1.28	16.49 ± 1.38	11.78 ± 0.97	6.49 ± 0.52	2.93 ± 0.25	0.99 ± 0.10	0.32 ± 0.04	0.05 ± 0.01	0.03 ± 0.01	
75	12.23 ± 1.96	17.09 ± 1.51	17.28 ± 1.38	15.90 ± 1.33	7.28 ± 0.61	2.77 ± 0.22	0.90 ± 0.08	0.26 ± 0.03	0.07 ± 0.02	0.02 ± 0.01		
90	12.49 ± 1.97	17.60 ± 1.54	15.95 ± 1.26	12.32 ± 1.02	4.13 ± 0.34	1.20 ± 0.09	0.31 ± 0.03	0.07 ± 0.01	0.02 ± 0.01			
105	14.92 ± 2.37	20.23 ± 1.77	15.58 ± 1.23	9.92 ± 0.83	2.51 ± 0.21	0.62 ± 0.06	0.11 ± 0.01	0.03 ± 0.01				
120	12.07 ± 1.92	16.01 ± 1.41	11.66 ± 0.93	6.47 ± 0.54	1.38 ± 0.12	0.28 ± 0.03	0.06 ± 0.01					
135	12.65 ± 2.01	16.91 ± 1.49	11.16 ± 0.89	5.48 ± 0.47	0.96 ± 0.09	0.16 ± 0.02	0.02 ± 0.01					
150	9.09 ± 1.45	13.24 ± 1.17	8.85 ± 0.71	3.99 ± 0.34	0.67 ± 0.06	0.11 ± 0.02	0.03 ± 0.01					

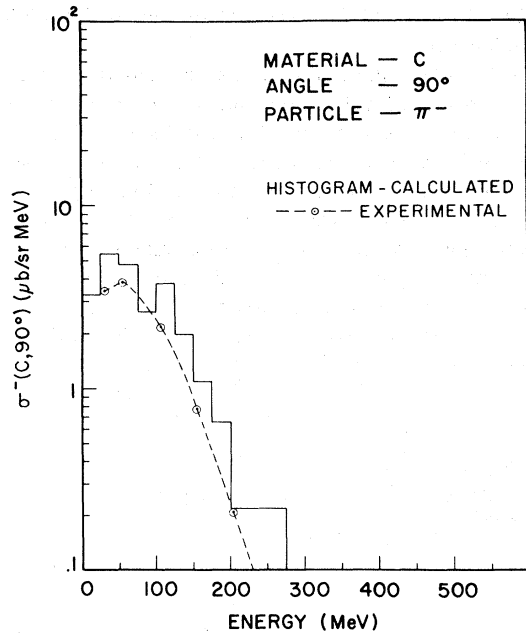


FIG. 12. $\sigma^-(\text{C}, 90^\circ)$. Histograms are cascade Monte Carlo calculations. Points are experimental data. Dashed line is to guide the eye.

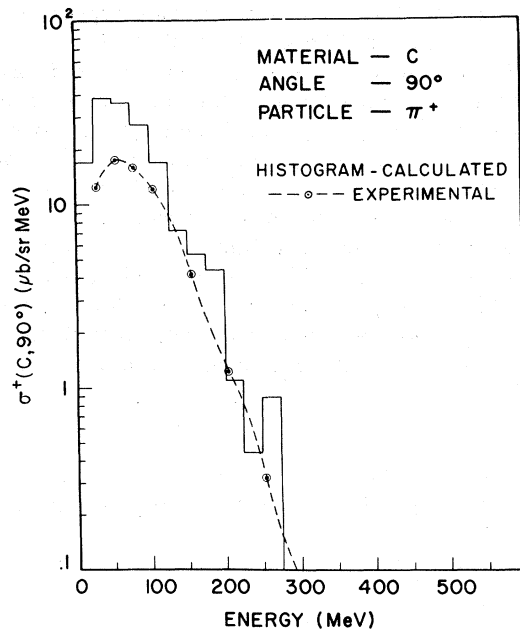


FIG. 13. $\sigma^+(\text{C}, 90^\circ)$. Histograms are cascade Monte Carlo calculations. Points are experimental data. Dashed line is to guide the eye.

TABLE XVI. Cross section for π^- from C in $\mu\text{b sr}^{-1}\text{MeV}^{-1}$.

Angle (deg)	Pion energy (MeV)											
	30	52	79	105	155	205	255	305	358	408	486	553
15	3.24 ± 0.53	3.89 ± 0.36	4.08 ± 0.33	5.01 ± 0.43	5.15 ± 0.43	4.96 ± 0.39	4.77 ± 0.40	3.62 ± 0.34	2.13 ± 0.21	0.69 ± 0.08	0.11 ± 0.02	
20	2.34 ± 0.39	3.39 ± 0.31	3.66 ± 0.30	4.47 ± 0.38	4.61 ± 0.38	4.52 ± 0.35	4.02 ± 0.34	2.97 ± 0.28	1.69 ± 0.17	0.54 ± 0.06	0.09 ± 0.02	
30	2.14 ± 0.36	3.43 ± 0.31	3.83 ± 0.31	4.67 ± 0.39	4.25 ± 0.35	3.98 ± 0.31	2.86 ± 0.24	1.83 ± 0.18	0.88 ± 0.09	0.26 ± 0.03	0.03 ± 0.01	
45	2.33 ± 0.37	3.01 ± 0.27	3.33 ± 0.27	3.78 ± 0.32	3.25 ± 0.27	2.27 ± 0.18	1.30 ± 0.11	0.58 ± 0.06	0.20 ± 0.02	0.03 ± 0.01		
60	2.52 ± 0.40	3.35 ± 0.29	3.37 ± 0.27	3.32 ± 0.28	2.13 ± 0.17	1.05 ± 0.08	0.43 ± 0.04	0.14 ± 0.01	0.04 ± 0.01			
75	2.92 ± 0.47	3.59 ± 0.32	3.39 ± 0.27	2.88 ± 0.24	1.27 ± 0.11	0.47 ± 0.04	0.14 ± 0.01	0.03 ± 0.01				
90	3.37 ± 0.54	3.80 ± 0.33	3.06 ± 0.24	2.17 ± 0.18	0.76 ± 0.06	0.20 ± 0.02	0.05 ± 0.01					
105	3.73 ± 0.59	3.88 ± 0.34	2.76 ± 0.22	1.77 ± 0.15	0.48 ± 0.04	0.10 ± 0.01	0.02 ± 0.01					
120	2.94 ± 0.47	3.25 ± 0.29	2.13 ± 0.17	1.18 ± 0.10	0.28 ± 0.02	0.05 ± 0.01						
135	2.99 ± 0.47	3.08 ± 0.27	1.97 ± 0.16	1.05 ± 0.09	0.20 ± 0.02	0.03 ± 0.01						
150	2.12 ± 0.34	2.50 ± 0.22	1.57 ± 0.13	0.76 ± 0.06	0.14 ± 0.01	0.03 ± 0.01						

scaling law. For 30-MeV π^+ it holds approximately for elements all the way from Be to Th.

Evidently the process of Δ formation and decay, which as we have seen dominates the pion production process in hydrogen at this energy, is strongly modified in the heavy elements. Since the Δ decays within a fermi or so to a π^+ nucleon, we expect the subsequent processes of pion absorption and scattering to be important. The $Z^{1/3}$ law for π^+ suggests that the π^+ which we measure are those produced peripherally, and which therefore tend to escape the nucleus with relatively little scattering or energy loss; hence the peaking in

nuclei of the π^+ at forward angles and at 250 MeV, as in hydrogen.

On the other hand, there are several indications that π^- production is somewhat more complicated than simple isobar formation and decay. The fact that the π^+/π^- ratio is much smaller than the isobar value, the preponderance of low-energy π^- , and rather flat angular distribution all suggest additional processes must be taking place. Since on the isobar model the π^0/π^- ratio is 6 for $N=Z$, π^0 formation and the charge-exchange reaction $\pi^0+n \rightarrow \pi^-+p$ is an important source of π^- . The additional step of charge-exchange scattering tends to

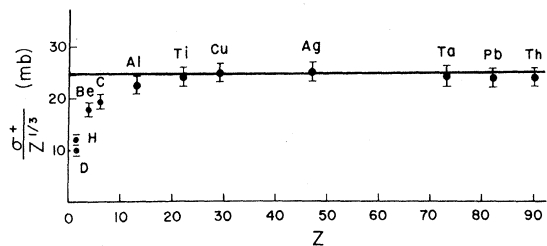
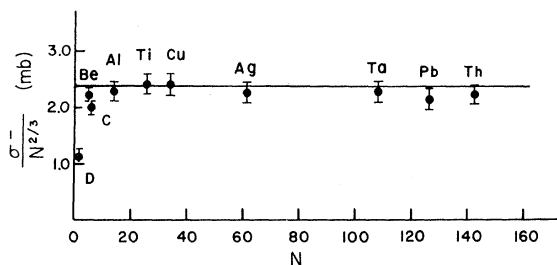
FIG. 14. π^+ total cross section $/Z^{1/3}$ vs Z .FIG. 15. π^- total cross section $/N^{2/3}$ vs N .

TABLE XVII. Cross section for π^+ from Al in $\mu\text{b}\text{sr}^{-1}\text{MeV}^{-1}$.

Angle (deg)	Pion energy (MeV)											
	30	52	79	105	155	205	255	305	358	408	486	553
15	9.94 ± 1.75	18.97 ± 1.78	24.15 ± 2.01	31.81 ± 2.73	38.00 ± 3.17	43.61 ± 3.43	51.17 ± 4.25	48.34 ± 4.57	37.73 ± 3.74	18.31 ± 2.07	3.99 ± 0.54	0.56 ± 0.11
20	13.85 ± 2.26	19.11 ± 1.72	22.54 ± 1.82	29.17 ± 2.46	33.53 ± 2.76	37.42 ± 2.91	41.11 ± 3.39	38.10 ± 3.59	26.87 ± 2.66	11.13 ± 1.26	2.81 ± 0.37	0.41 ± 0.08
30	12.88 ± 2.14	18.70 ± 1.71	23.24 ± 1.90	30.63 ± 2.59	32.94 ± 2.73	33.68 ± 2.64	32.58 ± 2.70	24.13 ± 2.29	12.62 ± 1.27	5.38 ± 0.62	0.87 ± 0.13	0.06 ± 0.03
45	13.47 ± 2.16	20.10 ± 1.78	22.98 ± 1.83	25.41 ± 2.12	23.78 ± 1.95	18.95 ± 1.48	13.00 ± 1.08	6.38 ± 0.61	2.83 ± 0.29	0.71 ± 0.09	0.11 ± 0.02	0.02 ± 0.01
60	15.06 ± 2.44	22.05 ± 1.97	23.88 ± 1.92	24.28 ± 2.04	17.37 ± 1.44	9.11 ± 0.73	4.58 ± 0.40	1.70 ± 0.18	0.49 ± 0.07	0.12 ± 0.03	0.03 ± 0.01	
75	18.80 ± 3.01	27.83 ± 2.46	25.25 ± 2.01	23.04 ± 1.93	10.97 ± 0.91	4.27 ± 0.35	1.60 ± 0.15	0.55 ± 0.07	0.18 ± 0.02	0.03 ± 0.01		
90	20.33 ± 3.21	28.77 ± 2.52	24.22 ± 1.91	18.94 ± 1.57	6.77 ± 0.56	2.01 ± 0.16	0.51 ± 0.04	0.17 ± 0.02	0.03 ± 0.01			
105	25.61 ± 4.07	31.99 ± 2.81	23.24 ± 1.85	15.59 ± 1.31	4.16 ± 0.35	1.07 ± 0.09	0.23 ± 0.03	0.06 ± 0.01				
120	21.22 ± 3.38	27.23 ± 2.40	18.94 ± 1.51	11.39 ± 0.96	2.34 ± 0.20	0.58 ± 0.06	0.11 ± 0.02	0.03 ± 0.01				
135	17.55 ± 2.78	25.70 ± 2.26	17.39 ± 1.38	9.07 ± 0.76	1.79 ± 0.16	0.36 ± 0.04	0.08 ± 0.01					
150	17.23 ± 2.74	22.19 ± 1.95	14.46 ± 1.15	7.23 ± 0.61	1.33 ± 0.12	0.29 ± 0.03	0.03 ± 0.01					

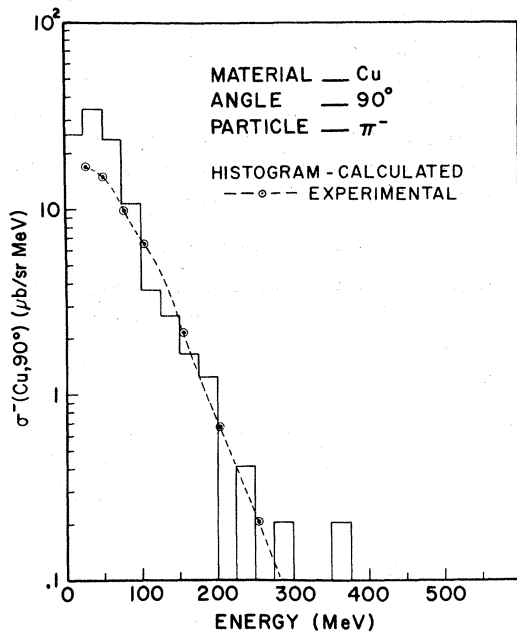
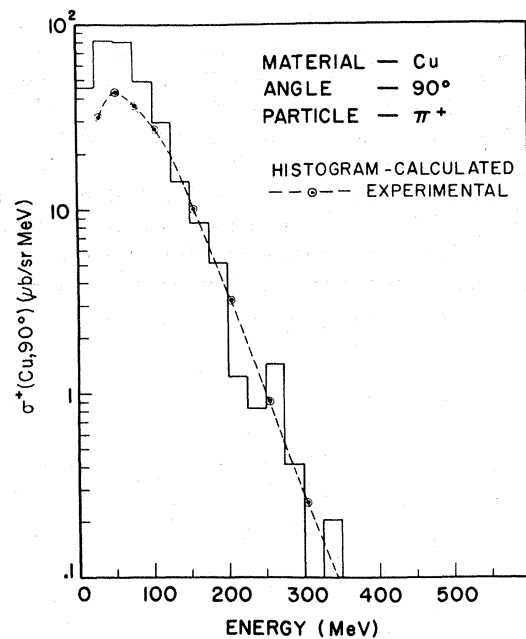
FIG. 16. Cascade Monte Carlo and experimental cross sections for $\text{Cu}(\pi^+, 90^\circ)$.FIG. 17. Cascade Monte Carlo calculations and experimental cross sections for $\text{Cu}(\pi^-, 90^\circ)$.

TABLE XVIII. Cross section for π^- from Al in $\mu\text{bsr}^{-1}\text{MeV}^{-1}$.

Angle (deg)	Pion energy (MeV)											
	30	52	79	105	155	205	255	305	358	408	486	553
15	6.60 ± 1.08	8.36 ± 0.75	8.13 ± 0.66	8.82 ± 0.75	8.58 ± 0.71	7.91 ± 0.63	7.24 ± 0.61	5.27 ± 0.50	3.31 ± 0.33	0.95 ± 0.11	0.26 ± 0.04	0.03 ± 0.01
20	6.16 ± 1.00	7.67 ± 0.69	7.17 ± 0.58	8.30 ± 0.71	7.35 ± 0.61	6.76 ± 0.53	6.13 ± 0.51	4.44 ± 0.42	2.58 ± 0.26	0.82 ± 0.10	0.19 ± 0.03	0.03 ± 0.01
30	5.75 ± 0.94	8.16 ± 0.73	7.85 ± 0.64	8.07 ± 0.68	7.03 ± 0.58	6.07 ± 0.48	4.76 ± 0.40	2.91 ± 0.28	1.39 ± 0.15	0.43 ± 0.05	0.08 ± 0.02	0.02 ± 0.01
45	5.64 ± 0.91	7.15 ± 0.64	6.56 ± 0.52	6.82 ± 0.57	5.19 ± 0.43	3.62 ± 0.29	2.16 ± 0.18	0.91 ± 0.09	0.39 ± 0.04	0.09 ± 0.02		
60	6.38 ± 1.01	7.45 ± 0.65	6.34 ± 0.50	5.87 ± 0.49	3.45 ± 0.29	1.80 ± 0.14	0.74 ± 0.06	0.27 ± 0.03	0.08 ± 0.01			
75	7.06 ± 1.13	7.85 ± 0.69	6.37 ± 0.51	5.20 ± 0.44	2.14 ± 0.18	0.81 ± 0.07	0.30 ± 0.03	0.08 ± 0.01	0.02 ± 0.01			
90	7.97 ± 1.26	7.97 ± 0.70	5.66 ± 0.45	3.95 ± 0.33	1.33 ± 0.11	0.43 ± 0.04	0.11 ± 0.01	0.03 ± 0.01				
105	8.53 ± 1.35	8.20 ± 0.72	5.27 ± 0.42	3.16 ± 0.26	0.85 ± 0.07	0.22 ± 0.02	0.04 ± 0.01					
120	7.38 ± 1.17	7.04 ± 0.62	4.20 ± 0.33	2.40 ± 0.20	0.53 ± 0.04	0.10 ± 0.01	0.02 ± 0.01					
135	7.15 ± 1.14	7.17 ± 0.63	4.07 ± 0.33	2.07 ± 0.18	0.44 ± 0.04	0.08 ± 0.01	0.02 ± 0.01					
150	5.32 ± 0.85	5.50 ± 0.49	3.07 ± 0.25	1.55 ± 0.13	0.29 ± 0.03	0.06 ± 0.01						

lower the energy, broaden the angular distribution, decrease the π^+/π^- ratio, and make the total cross section more nearly proportional to the nuclear area times (N/A) , or roughly $N^{2/3}$. The partial success of the cascade Monte Carlo calculations, which embody these ideas, also testifies to their essential correctness.

Sternheim and Silbar³³ have calculated the π production based on the above ideas, plus the effects of π absorption by the nucleus. The approach differs from earlier treatments by Margolis²⁴ and Beder³⁴ in dropping the forward-scattering as-

sumption and in including the charge-exchange scattering. They obtain fairly good predictions of the spectra and the total cross sections.³³

The success of these models indicates that π production in nuclei can be generally understood on the basis of relatively simple considerations, and that details of nuclear structure play a minor role in π production at this energy.

ACKNOWLEDGMENTS

We thank James Vale and the cyclotron staff for their constant support, Edwin McLaughlin for the

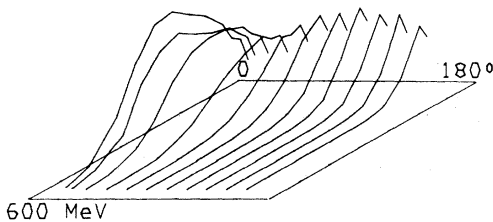


FIG. 18. Experimental distribution for π^+ from Cu. Solid lines are polygons through the data points.

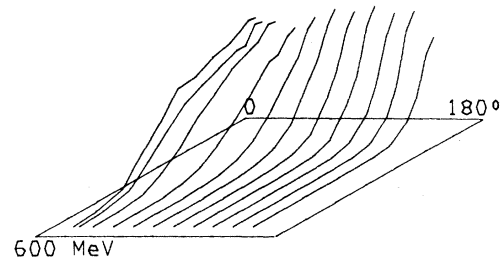


FIG. 19. Experimental distribution for π^- from Cu. Solid lines are polygons through the data points.

TABLE XIX. Cross section for π^- from Cu in $\mu\text{bsr}^{-1}\text{MeV}^{-1}$.

Angle (deg)	Pion energy (MeV)											
	30	52	79	105	155	205	255	305	358	408	486	553
15	14.71 ± 2.72	28.25 ± 2.73	31.93 ± 2.77	42.06 ± 3.70	52.39 ± 4.44	58.51 ± 4.67	65.14 ± 5.48	63.28 ± 6.03	46.96 ± 4.71	24.23 ± 2.78	5.66 ± 0.79	1.09 ± 0.22
20	17.23 ± 2.99	29.72 ± 2.78	34.51 ± 2.89	40.42 ± 3.50	43.08 ± 3.64	47.86 ± 3.81	53.54 ± 4.49	48.95 ± 4.66	36.40 ± 3.64	14.40 ± 1.67	3.86 ± 0.55	0.52 ± 0.12
30	18.40 ± 3.07	30.22 ± 2.75	34.53 ± 2.82	40.85 ± 3.47	44.78 ± 3.72	45.49 ± 3.57	42.51 ± 3.54	32.25 ± 3.07	16.69 ± 1.68	7.15 ± 0.83	1.23 ± 0.19	0.09 ± 0.04
45	18.84 ± 3.08	30.68 ± 2.75	31.81 ± 2.57	35.55 ± 3.00	31.78 ± 2.63	25.86 ± 2.03	17.71 ± 1.49	9.30 ± 0.90	4.28 ± 0.45	1.11 ± 0.15	0.16 ± 0.04	0.03 ± 0.01
60	24.91 ± 4.00	36.33 ± 3.22	34.16 ± 2.74	35.27 ± 2.96	23.09 ± 1.91	13.15 ± 1.04	6.17 ± 0.53	2.63 ± 0.27	1.00 ± 0.12	0.20 ± 0.04	0.08 ± 0.02	
75	31.12 ± 4.96	41.97 ± 3.70	37.57 ± 2.99	33.35 ± 2.79	15.81 ± 1.31	6.73 ± 0.54	2.43 ± 0.22	0.80 ± 0.09	0.28 ± 0.04	0.06 ± 0.02		
90	31.01 ± 4.92	43.17 ± 3.79	35.78 ± 2.83	26.97 ± 2.25	9.77 ± 0.81	3.11 ± 0.25	0.89 ± 0.08	0.25 ± 0.03	0.07 ± 0.02			
105	36.61 ± 5.81	46.21 ± 4.06	36.18 ± 2.87	23.53 ± 1.97	6.69 ± 0.56	1.75 ± 0.15	0.44 ± 0.05	0.11 ± 0.02	0.02 ± 0.01			
120	33.62 ± 5.35	42.75 ± 3.77	30.53 ± 2.44	18.73 ± 1.58	4.12 ± 0.36	1.01 ± 0.10	0.16 ± 0.03	0.04 ± 0.01				
135	30.06 ± 4.78	42.73 ± 3.76	28.27 ± 2.25	15.35 ± 1.29	3.10 ± 0.27	0.68 ± 0.07	0.08 ± 0.02	0.02 ± 0.01				
150	27.89 ± 4.44	36.30 ± 3.20	24.35 ± 1.95	12.58 ± 1.07	2.58 ± 0.23	0.46 ± 0.06	0.08 ± 0.02	0.02 ± 0.01				

design of the hydrogen system, Victor Brady for assistance with magnet computations, and Stanley Curtis for assistance during the early phases of the experiment. We thank R. Silbar and M. Sternheim for many illuminating discussions. We thank Robert Rajala and David Jones for interfacing the PDP-8, and Sally Shlaer for assistance in the PDP-8 programming. One of us (D. E. Nagle) wishes to acknowledge the hospitality of the Aspen Center for Physics, where much of this paper was written.

APPENDIX A

1. Ion-Chamber Integrators

The electronic integrators used during the experiment were an ORTEC model 439 and a BIC model 1000. The BIC was used with the helium chamber for all data-taking runs, and the current range selected was calibrated to better than 1% at the LASL Standards Laboratory. The calibration

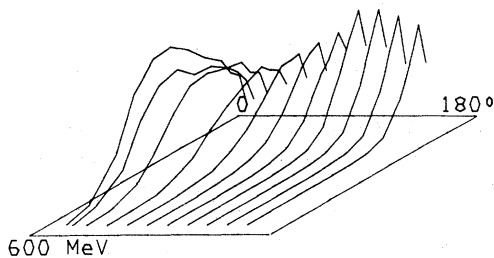
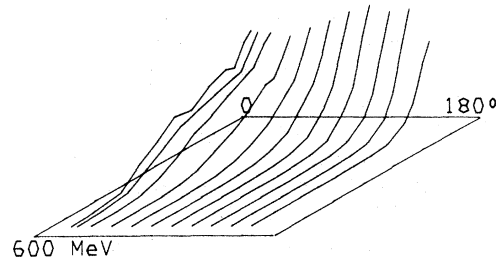
FIG. 20. Experimental distributions for π^+ from Th.FIG. 21. Experimental distributions for π^- from Th.

TABLE XX. Cross section for π^- from Cu in $\mu\text{bsr}^{-1}\text{MeV}^{-1}$.

Angle (deg)	Pion energy (MeV)											
	30	52	79	105	155	205	255	305	358	408	486	553
15	15.71 ± 2.55	15.91 ± 1.44	14.87 ± 1.22	14.02 ± 1.21	13.40 ± 1.13	11.97 ± 0.96	11.70 ± 0.99	8.07 ± 0.78	4.90 ± 0.51	1.46 ± 0.18	0.31 ± 0.06	0.06 ± 0.02
20	15.05 ± 2.41	15.34 ± 1.37	12.92 ± 1.05	13.00 ± 1.10	11.87 ± 0.99	10.74 ± 0.84	9.38 ± 0.79	6.72 ± 0.65	3.82 ± 0.38	1.25 ± 0.16	0.28 ± 0.05	0.03 ± 0.01
30	15.11 ± 2.42	15.32 ± 1.36	13.56 ± 1.09	13.06 ± 1.10	11.72 ± 0.97	9.39 ± 0.74	7.33 ± 0.62	4.35 ± 0.42	2.09 ± 0.22	0.62 ± 0.08	0.12 ± 0.02	0.02 ± 0.01
45	14.29 ± 2.28	13.51 ± 1.20	11.65 ± 0.94	11.31 ± 0.95	8.21 ± 0.69	5.46 ± 0.43	3.24 ± 0.28	1.44 ± 0.15	0.59 ± 0.07	0.14 ± 0.03	0.03 ± 0.01	
60	15.84 ± 2.52	14.54 ± 1.28	11.26 ± 0.90	9.38 ± 0.79	5.62 ± 0.47	2.78 ± 0.22	1.16 ± 0.11	0.43 ± 0.04	0.14 ± 0.02	0.03 ± 0.01		
75	17.10 ± 2.72	15.01 ± 1.33	10.89 ± 0.87	8.65 ± 0.73	3.48 ± 0.29	1.34 ± 0.11	0.48 ± 0.05	0.15 ± 0.02	0.06 ± 0.01			
90	16.71 ± 2.65	14.65 ± 1.29	9.55 ± 0.76	6.30 ± 0.53	2.07 ± 0.17	0.65 ± 0.06	0.20 ± 0.02	0.05 ± 0.01				
105	17.46 ± 2.77	15.05 ± 1.33	8.67 ± 0.69	5.30 ± 0.45	1.39 ± 0.12	0.31 ± 0.03	0.08 ± 0.01	0.03 ± 0.01				
120	16.52 ± 2.62	13.72 ± 1.21	7.51 ± 0.60	3.97 ± 0.34	0.93 ± 0.08	0.18 ± 0.02	0.04 ± 0.01					
135	16.80 ± 2.67	14.48 ± 1.28	7.15 ± 0.58	3.31 ± 0.29	0.68 ± 0.07	0.13 ± 0.02	0.03 ± 0.01					
150	12.96 ± 2.06	10.99 ± 0.97	5.36 ± 0.43	2.63 ± 0.23	0.44 ± 0.04	0.09 ± 0.01	0.02 ± 0.01					

was checked occasionally during the experiment, and no drift was observed.

2. Argon-Chamber Calibrations

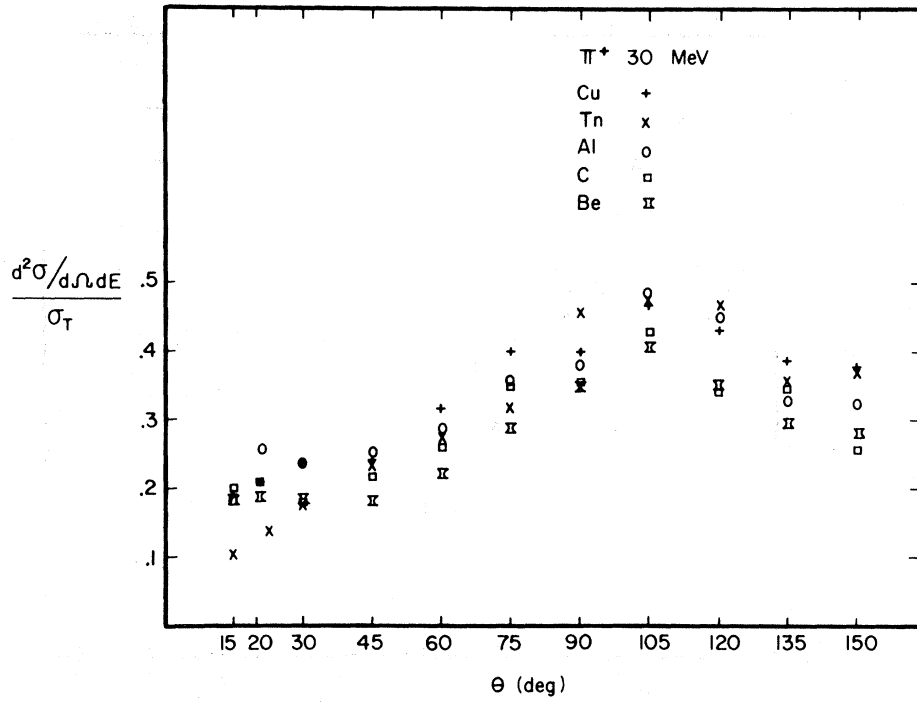
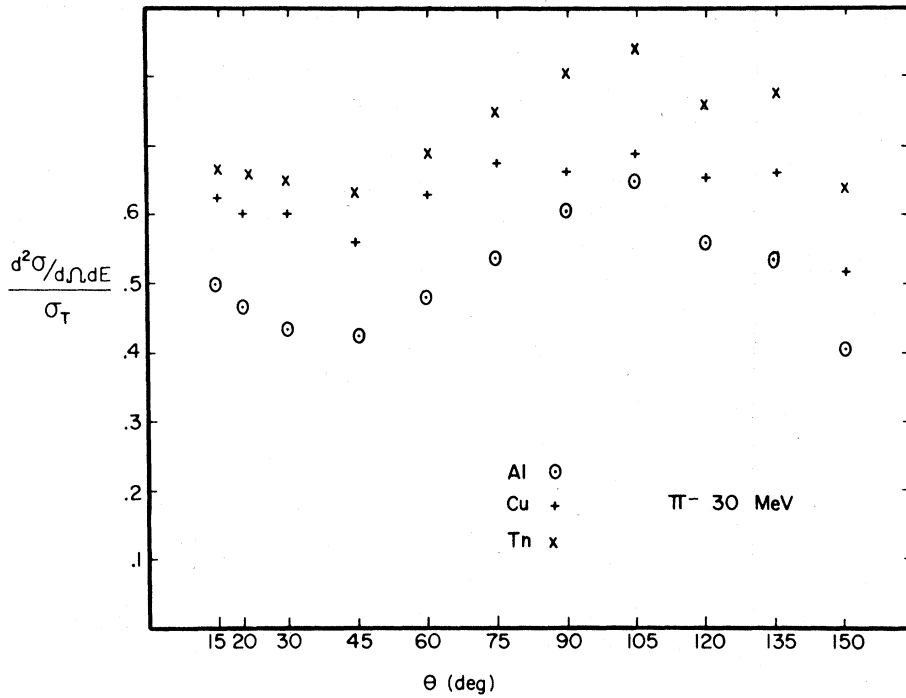
A 5-cm ion chamber filled with 96% argon and 4% CO₂ (by weight) to an absolute pressure of 889 Torr at 22 °C was used as an absolute beam monitor. The gain of this chamber was computed from the energy deposit per ion pair data of Bakker and Segrè,³⁵ obtained by comparing the ionization current produced by 340-MeV protons with beam current monitored in a Faraday cup. By scaling to the conditions of our experiment, we obtained a calibration based on the Bakker and Segrè measurement. The ionization potential of our gas mixture was determined from the Ar data of Bakker and Segrè and the CO₂ data of Hine and Brownell.³⁶ The (dE/dx weighted average) ionization potential is 25.85 eV per ion pair. To preserve the accuracy of the Bakker and Segrè data we took their value of dE/dx , namely, 4.02 keV/cm for Ar gas at 15 °C and 760 Torr, and corrected this to 740 MeV and an Ar-CO₂ mixture, using data from Janni.³⁷ The gain of the argon chamber was calculated for our temperature and pressure to be $G = 669$. The gain

calculation should have the same accuracy as the Bakker and Segrè data, namely, $\pm 1\%$, since all factors except beam energy were measured with considerably greater precision. If the assumed beam energy were changed to 720 MeV, the calculated gain would increase by 1%.

The actual calibration consisted of placing the Ar-CO₂ chamber at the position of the production target, then comparing the charge collected in the two chambers. In order that this calibration be independent of the integrator gains, this measurement was made, then repeated with the integrators interchanged. The helium-chamber gain was then calculated from the relation

$$G = 669 \frac{\text{He(BIC)}}{\text{Ar-CO}_2(\text{ORTEC})} \times \frac{\text{He(ORTEC)}}{\text{Ar-CO}_2(\text{BIC})}$$

The He gain defined in this way was a function of beam current because of recombination effects in the Ar-CO₂ chamber; hence the measurement was made at several beam currents and the "plateau" value of the gain was used. The gain data for the two target positions are given in Table XXIII. The best estimate of the He-chamber gain from these measurements is 178 ± 5 .

FIG. 22. $(d^2\sigma/d\Omega dE)/\sigma_T$ for 30-MeV π^+ .FIG. 23. $(d^2\sigma/d\Omega dE)/\sigma_T$ for 30-MeV π^- .

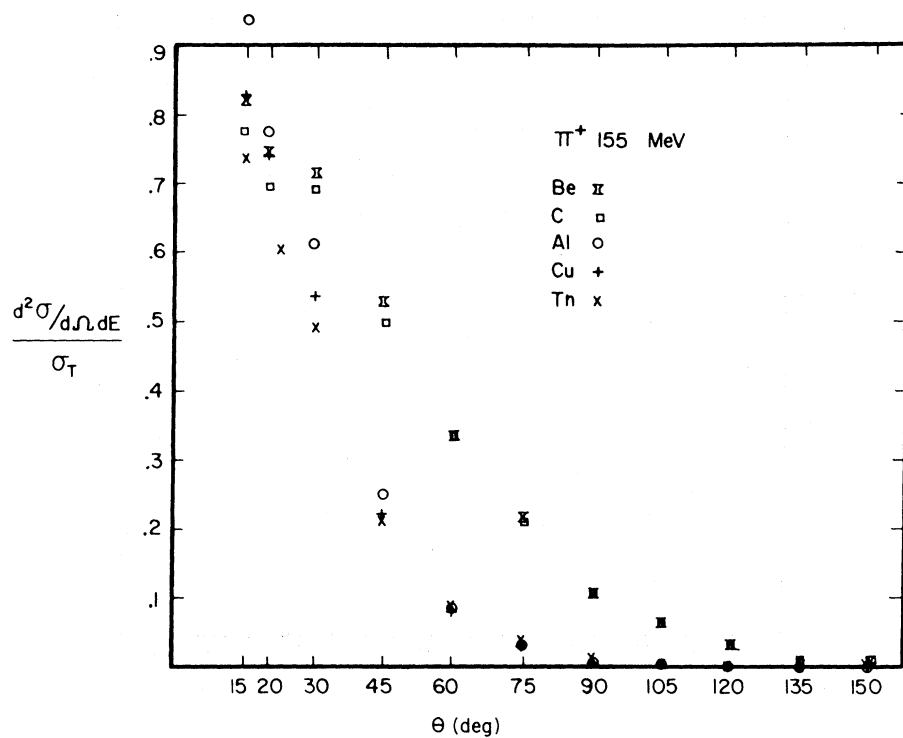
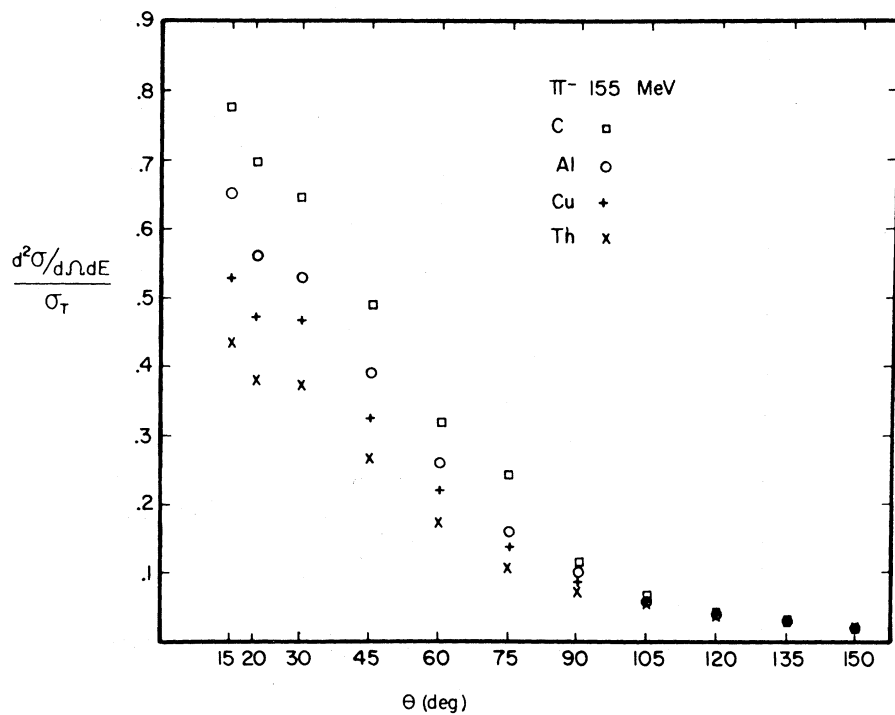
FIG. 24. $(d^2\sigma/d\Omega dE)/\sigma_T$ for 155-MeV π^+ .FIG. 25. $(d^2\sigma/d\Omega dE)/\sigma_T$ for 155-MeV π^- .

TABLE XXI. Cross section for π^+ from Pb in $\mu\text{b sr}^{-1}\text{MeV}^{-1}$.

Angle (deg)	Pion energy (MeV)											
	30	52	79	105	155	205	255	305	358	408	486	553
15	19.75 ± 3.60	31.51 ± 3.09	36.82 ± 3.21	49.11 ± 4.34	57.53 ± 4.92	64.43 ± 5.17	75.86 ± 6.39	73.57 ± 7.02	57.49 ± 5.76	27.27 ± 3.14	4.82 ± 0.71	0.89 ± 0.21
20	16.21 ± 3.06	31.96 ± 3.09	37.04 ± 3.18	45.19 ± 3.98	50.72 ± 4.33	54.46 ± 4.38	61.85 ± 5.23	59.36 ± 5.67	43.69 ± 4.40	18.86 ± 2.19	4.19 ± 0.61	0.31 ± 0.12
30	17.76 ± 3.04	36.24 ± 3.32	39.86 ± 3.29	48.89 ± 4.18	51.10 ± 4.26	53.30 ± 4.20	50.90 ± 4.26	38.56 ± 3.67	20.65 ± 2.09	8.11 ± 0.96	1.29 ± 0.22	0.16 ± 0.06
45	23.35 ± 3.86	37.96 ± 3.43	39.62 ± 3.23	44.02 ± 3.74	40.00 ± 3.33	32.24 ± 2.56	21.54 ± 1.83	12.33 ± 1.20	5.27 ± 0.56	1.39 ± 0.20	0.20 ± 0.06	0.05 ± 0.02
60	27.59 ± 4.48	44.82 ± 4.00	44.76 ± 3.60	45.03 ± 3.79	29.76 ± 2.48	16.67 ± 1.34	8.47 ± 0.74	3.58 ± 0.37	1.48 ± 0.18	0.23 ± 0.05	0.08 ± 0.03	0.05 ± 0.02
75	37.50 ± 6.04	56.41 ± 5.01	51.21 ± 4.11	43.02 ± 3.62	21.96 ± 1.84	9.14 ± 0.76	3.55 ± 0.34	1.09 ± 0.13	0.45 ± 0.07	0.05 ± 0.03	0.03 ± 0.01	0.02 ± 0.01
90	48.70 ± 7.74	68.72 ± 6.04	55.85 ± 4.43	44.18 ± 3.69	16.86 ± 1.40	5.46 ± 0.45	1.74 ± 0.17	0.43 ± 0.06	0.19 ± 0.03	0.04 ± 0.02		
105	53.07 ± 8.47	74.35 ± 6.55	55.21 ± 4.40	39.42 ± 3.31	12.00 ± 1.02	2.95 ± 0.27	0.76 ± 0.09	0.17 ± 0.04	0.05 ± 0.02			
120	48.14 ± 7.65	68.54 ± 6.03	48.99 ± 3.89	31.42 ± 2.63	7.74 ± 0.66	1.77 ± 0.16	0.33 ± 0.05	0.07 ± 0.02	0.03 ± 0.01			
135	38.22 ± 6.11	69.39 ± 6.11	47.63 ± 3.80	28.15 ± 2.37	6.63 ± 0.58	1.33 ± 0.14	0.30 ± 0.05	0.07 ± 0.02	0.02 ± 0.01			
150	37.83 ± 6.04	64.14 ± 5.65	43.87 ± 3.50	23.70 ± 2.00	5.05 ± 0.44	0.84 ± 0.09	0.16 ± 0.04	0.04 ± 0.01				

3. Foil Calibration of Beam Monitors

The foil activation studies were carried out in collaboration with the LBL Berkeley Health Physics Group. The activities studied were ^{149}Tb , ^{24}Na , and ^7Be and ^{11}C , from gold, aluminum, and polyethylene, respectively. Only the results from the irradiation in which the three foil materials were simultaneously bombarded by 730-MeV protons will be reported, although a 5-min irradiation of polyethylene was performed to establish the $^7\text{Be}/^{11}\text{C}$ production ratio.

To account for particle recoil effects each foil was covered, front and back, with like material for the irradiation. The total interaction probability in the foil stack for 730-MeV protons was about 1%. The error due to secondary interactions is estimated to be less than 1%.

The results of the activation study are summarized in Table XXIV, giving the cross sections³⁸ at 730 MeV used to calculate the average current and the calculated gain of the He chamber. During the 4-h irradiation the beam current was sufficiently steady so that no time-dependent production-rate corrections were necessary.

The mean value 195 of the He-ion-chamber gain differs from the value (178) from the Ar-CO₂ calibration. The discrepancy could be explained by saying that the activation cross sections used were too small; the literature values used have quoted errors between 5% and 13%. Errors due to secondary interactions tend to increase the current and reduce the calculated ion-chamber gain. Radioautographs of the irradiated foils gave no indication of beam missing the foils. The counting statistics contributed ±3% error. In computing cross sections we adopted the value 183 for the He-ion-chamber gain.

APPENDIX B: PION-DECAY CORRECTIONS (PIMU)

The measured fluxes of pions must be corrected for pion decays in flight to obtain the fluxes emitted at the production target. The attenuation can be calculated from the flight paths from the target to the final detector (S_4) in each channel. In addition, muons arising from pion decays can be detected with nearly 100% efficiency. It was necessary therefore to estimate what fraction of the par-

TABLE XXII. Cross section for π^- from Pb in $\mu\text{b sr}^{-1}\text{MeV}^{-1}$.

Angle (deg)	Pion energy (MeV)											
	30	52	79	105	155	205	255	305	358	408	486	553
15	37.31 ± 5.99	30.68 ± 2.77	26.79 ± 2.20	25.28 ± 2.17	22.71 ± 1.92	20.60 ± 1.66	18.97 ± 1.62	13.94 ± 1.35	8.29 ± 0.85	2.06 ± 0.27	0.55 ± 0.09	0.13 ± 0.03
20	34.29 ± 5.49	28.76 ± 2.58	25.11 ± 2.04	24.75 ± 2.10	20.88 ± 1.75	19.18 ± 1.52	16.12 ± 1.36	11.41 ± 1.10	6.02 ± 0.62	1.85 ± 0.23	0.39 ± 0.07	0.07 ± 0.02
30	37.54 ± 5.99	30.91 ± 2.75	24.89 ± 2.01	24.09 ± 2.04	19.82 ± 1.65	16.83 ± 1.33	12.34 ± 1.04	7.13 ± 0.69	3.37 ± 0.35	1.00 ± 0.13	0.17 ± 0.04	
45	32.84 ± 5.23	29.63 ± 2.62	21.89 ± 1.76	20.15 ± 1.70	14.44 ± 1.20	9.94 ± 0.79	5.13 ± 0.44	2.40 ± 0.24	0.94 ± 0.11	0.27 ± 0.04		
60	36.19 ± 5.74	29.50 ± 2.60	20.76 ± 1.65	17.27 ± 1.45	8.86 ± 0.74	4.69 ± 0.37	2.07 ± 0.18	0.83 ± 0.09	0.31 ± 0.04	0.04 ± 0.01		
75	39.81 ± 6.32	30.21 ± 2.67	19.58 ± 1.57	14.79 ± 1.25	5.79 ± 0.49	2.18 ± 0.19	0.81 ± 0.08	0.27 ± 0.04	0.08 ± 0.02			
90	44.18 ± 6.99	31.84 ± 2.80	19.33 ± 1.54	12.03 ± 1.01	3.93 ± 0.33	1.31 ± 0.11	0.37 ± 0.04	0.13 ± 0.02	0.03 ± 0.01			
105	49.11 ± 7.77	32.62 ± 2.87	17.71 ± 1.41	9.77 ± 0.83	2.57 ± 0.22	0.70 ± 0.07	0.20 ± 0.03	0.05 ± 0.01				
120	39.35 ± 6.23	28.53 ± 2.51	15.25 ± 1.22	7.74 ± 0.66	1.73 ± 0.16	0.42 ± 0.04	0.08 ± 0.01	0.02 ± 0.01				
135	38.22 ± 6.07	29.25 ± 2.58	14.16 ± 1.14	7.06 ± 0.61	1.39 ± 0.13	0.30 ± 0.04	0.08 ± 0.02					
150	31.93 ± 5.06	24.10 ± 2.13	11.74 ± 0.95	5.39 ± 0.47	0.92 ± 0.09	0.23 ± 0.03	0.04 ± 0.01					

ticles detected as pions were, in fact, muons.

Let N_i be the number of particles detected as pions in channel i , and let P_i and M_i be the actual number of pions and muons comprising N_i ($N_i = P_i + M_i$). These quantities can be related to the desired laboratory cross sections and experimental parameters as follows:

$$\begin{aligned}
 P_i(\theta) &= n_p n_t \Delta\Omega \int_0^\infty R_i(p) \frac{d^2\sigma(\theta, p)}{dp d\Omega} \exp\left(-\frac{t_i}{T_i}\right) dp \\
 &= n_p n_t \Delta\Omega \Delta p_i \frac{d^2\sigma(\theta, p_i)}{dp d\Omega} D_i \\
 &= CD_i \sigma_i \Delta p_i,
 \end{aligned}$$

TABLE XXIII. He-ion-chamber gain from Ar-CO₂-chamber comparison.

Backward-angle setup		Forward-angle setup	
He current	He gain	He current	He gain
1.4×10^{-9}	178.0	3×10^{-8}	178.5
3.2×10^{-9}	178.0	2.5×10^{-7}	180.9
1.4×10^{-8}	178.5		
1.3×10^{-7}	180.1		
1.4×10^{-6}	199.4		

where we have assumed that $d^2\sigma/dpd\Omega$ is constant over the momentum interval Δp_i (full width at half-maximum), and have replaced the momentum-resolution function $R_i(p)$ by a rectangular function of width Δp_i . The quantities n_p and n_t are the number of protons incident on the target and the number of target nuclei per square cm as viewed by the proton beam, respectively. The exponential decay factor is represented by D_i and depends on the length of the channel and its central momentum p_i . Similarly

$$\begin{aligned}
 M_i(\theta) &= n_p n_t \Delta\Omega \int_0^\infty \frac{d^2\sigma(\theta, p)}{dp d\Omega} F(p_i, p) dp \\
 &= C \sum_j F_{ij} \sigma_j q_j,
 \end{aligned}$$

where $F(p_i, p)$ is the fractional probability that a pion of momentum p decays into a muon which is detected in channel i . We replace the integral with a sum over average quantities evaluated at each of the 12 channel momenta. F_{ij} is an abbreviation for $F(p_i, p_j)$. The quantities q_j are the momentum intervals over which the quantities F and σ are averaged [i.e., $q_j = \frac{1}{2}(p_{j+1} - p_{j-1})$]. We need not consider momenta below the lowest channel momentum, since the momentum of the muons arising

TABLE XXIV. Calibration of ion-chamber gain from activation study.

Target	Activity	Production cross section (mb)	Average current (nA)	He-ion-chamber gain
CH ₂	¹¹ C	29.8	21.8	192
	⁷ Be	11.0	20.9	200
Al	²⁴ Na	10.8	20.9	200
Au	¹⁴⁹ Tb	0.21	22.3	188
			Average	195

from pion decay have a momentum range from slightly more than the momentum of the pion to roughly half the pion's momentum. Also, at the high-momentum end of the pion spectrum, kinematics does not permit pions to be produced with momenta higher than that of our highest-momentum channel at any angle.

Therefore, we can write for any particular target and spectrometer angle

$$\begin{aligned}
 N_i &= P_i + M_i \\
 &= CD_i \sigma_i \Delta p_i + C \sum_j F_{ij} \sigma_j q_j \\
 &= C \sum_j [\delta_{ij} D_j \Delta p_j + F_{ij} q_j] \sigma_j .
 \end{aligned}$$

Letting

$$f_{ij} = \frac{F_{ij} q_j}{\Delta p_i}$$

and defining an observed cross section $\bar{\sigma}_i = N_i / C \Delta p_i$ we can write

$$\bar{\sigma}_i = \sum_j (\delta_{ij} D_j + f_{ij}) \sigma_j = \sum_j G_{ij} \sigma_j .$$

Thus, the desired cross sections can be obtained from the inverse of the matrix G :

$$\sigma_i = \sum_j G^{-1}_{ij} \bar{\sigma}_j .$$

The pion-decay probabilities f_{ij} (which are independent of angle and target) were calculated via a Monte Carlo technique which traced muons arising from pion decays at a succession of fixed distances from the target. This calculation was carried out for each channel over the full range of pion energies and averaging over the possible pion decay points. The initial pion directions at the target were chosen over a sufficiently large solid angle so that all possible decay muons that could enter the spectrometer were included. The effect of the beam collimator was also included, and had the effect of eliminating most of the possible large-angle pion decay points except those very close to the target. The trajectories through the spectrometer were calculated as circular orbits with edge

focusing within a wedge-shaped field region.

The 12-by-12 inverse G matrix was calculated before the experiment was set up for a geometry very similar to that actually used. The off-diagonal matrix elements of G are typically less than 3% of the diagonal elements. For a typical channel, only three or four terms contribute, so that the correction due to muons arising from pion decay is of the order of 10%. It is estimated that the upper limit of the error due to this correction is 50% of the correction.

The inverse matrix was stored in the PDP-8 so that the decay correction could be applied immediately to the results of each run. After the data-taking stage of the experiment was completed, a recalculation of the model wedge magnet geometry was made, and the new results agreed quite closely with those used in the original calculation. In addition, a new calculation of the channel-10 correction was made. The correction appears to be a bit larger than that calculated earlier, but would decrease the channel-10 cross sections (assuming a flat pion-production spectrum) by only 1.9%.

The code also calculated the energy and time of flight of muons detected as pions. The result, which was available early in the experimental design stage, indicated that it would be difficult to distinguish between pions and muons. Therefore, the discrimination windows were set generously so that the muons would be detected as pions with full efficiency. However, knowing the muon energies in detail from the calculation allowed a crude check of the validity of the calculated correction to be made by comparing the calculated output spectrum from a totally absorbing Čerenkov counter with an experimental measurement. Looking with a water Čerenkov detector in the 150-MeV pion energy channel, a high-pulse-height tail was observed arising from muons extending beyond the pulse-height peak arising from pions. The ratio of pulses with pulse heights greater than twice the average pion pulse height was observed to be 0.075. The ratio calculated by converting the calculated energy spectrum into a pulse-height spectrum was 0.062. It is believed that this result in-

icates that the correction for muons arising from pion decay is satisfactory within the errors stated above.

APPENDIX C: MULTIPLE-COULOMB-SCATTERING CORRECTIONS AND MOMENTUM DETERMINATION

A computer program entitled MULCOS was written to calculate the channel central momenta and momentum resolution function from the measured positions and to estimate the possible loss of particles due to multiple Coulomb scattering.

The MULCOS program incorporated the FOCUS program as a subroutine so that trajectories could be calculated from the measured magnetic field. Central momenta for each channel were calculated from the measured counter positions via a successive approximation search mode of MULCOS. The resulting momenta agreed with 1.3% of the momenta originally desired for channels 0 through 8. The momenta of channels 9, 10, and 11 changed by +3.3%, +1.9%, and -7.5%, respectively, the latter change being due to the counter position change. The increased sensitivity of channel momentum to position in the lower-momentum channels is expected, since the momentum dispersion is smaller in these channels.

Momentum resolution (full width at half-maximum) was determined from the calculated dispersion at the S_3 counter width in the bending plane. The momentum resolution was also checked by using the MULCOS program in a mode which permitted the variation of the trajectory momentum for a given geometry, which in effect is equivalent to determining the dispersion exactly. The MULCOS program was particularly useful in determining the momentum resolution function of channel 11, since the minimum accepted momentum was determined by counter S_4 rather than S_3 . The calculated channel central momenta and momentum interval accepted are listed Table I.

The spectrometer was designed so that the counters S_0 and S_1 would be the defining apertures. The width of S_3 in the bending plane would then determine the momentum cut accepted in each channel. All other counter dimensions (S_2 , S_3 height, S_4) were designed to be so generous that no particle could miss them unless it were multiple-Coulomb-scattered through an angle equal to several mean projected scattering angles in one of the counters. The adequacy of the design was verified by using MULCOS, which calculated these effects using the Monte Carlo technique as follows.

The production target and each counter were specified by eight parameters, three being used to

specify the location of the counter, two specifying their rectangular area, two specifying their thickness and atomic number, and one specifying the angular orientation of their normals from the horizontal plane. In addition, the air or helium in the path of the beam could be lumped into six "apertures," which allowed one to take into account the scattering from these materials. The effect of the collimator hole in the shield wall was accounted for. For the geometry specified, charged particles were started at random positions in the target and aimed at randomly chosen points in the spectrometer entrance aperture defined by S_0 and S_1 . Vertical and horizontal transport matrices were calculated from aperture to aperture, and used to transfer particle vectors one by one through the system. At each aperture, the position of the particle was checked to see if it passed through the aperture or had missed it. The tracing continued until the particle successfully entered the Plexiglas Čerenkov counter or missed one of the apertures. The first tracing of each particle ignored any multiple scattering. To evaluate the scattering effects, each particle was restarted with the same initial conditions. At each aperture, a scattering angle appropriately randomly distributed for the particle being traced and for the thickness and atomic number of the material in the aperture was added to the particle's angle, and the tracing continued. The multiple-Coulomb-scattering formulation of Marion and Zimmerman³⁹ was used. Again the particle was traced until it reached the final detector or missed an aperture.

Calculation of the transmission was made for each channel with and without multiple scattering. The transmission was 100% (standard deviation less than 1%) with multiple scattering ignored. With multiple scattering turned on, the transmission was also 100%, with somewhat poorer statistics in the low-momentum channels. (Actual numbers for transmission with multiple scattering to no multiple scattering were $1.08 \pm .06$ for channel 11, and 1.00 ± 0.02 for channel 10. These numbers assume the presence of a 4-ft-long He-filled bag just ahead of S_0 .) We conclude that we do not need to correct for any losses due to multiple Coulomb scattering in the scintillation counters and the target.

APPENDIX D: CROSS—Cross Section Analysis Program

The final cross sections were calculated on a CDC 6600 computer with the program CROSS. Input data were obtained from the paper tapes generated by the PDP-8 computer, which were transcribed to punched cards to facilitate manipulation and cor-

rections. The program consisted of ten parts.

(1) *Energy parameters* read in the central momenta and momentum widths of the 12 momentum channels defined by the spectrometer. Corresponding kinematical quantities are calculated and stored for subsequent use.

(2) A *CH range table* permits entry of range-energy tables for the plastic scintillator material for subsequent calculation of pion and proton energies at any point throughout the particle trajectories.

(3) A *decay matrix* section reads in the matrix $F(I, J)$ described in Appendix B.

(4) An *inscattering* section reads in the inscattering corrections.

(5) A *background* section reads in data from a run defined as a background run. The input cards are checked for consistency in run numbers, the products of the dE/dx and time-of-flight efficiencies are checked for each particle and channel, and, if the efficiency does not exceed 98%, a warning statement is printed.

(6) A *run data* section reads in data concerning various kinematical quantities for pions and protons referred to the center of the production target. The characteristics of the target and a range-energy table for the target material, then computes vari-

(7) A *foreground* section reads in data from a run defined as a foreground run. The input cards are checked for consistency of target, angle, etc., with the most recently read-in background run. The detection efficiencies are again checked as described above for the background run. Cross sections are calculated, correcting for attenuation of the incident protons by the target and for atten-

uation of the existing protons and pions by the target and other material between the target and the final detector in each channel. The background is also subtracted and background errors appropriately compounded. Note that the momentum widths used in calculating the cross sections are not simply those defined by the spectrometer but rather those effective at the target center. Corrections for pion decay and acceptance of muons from pion decay are applied to the pion data. Next, the inscattering corrections are applied to the pion cross sections. The electron cross-section results are given as ratios relative to the corrected pion cross sections. Thus, these numbers should approximate roughly the number of electrons relative to pions of the same momentum produced at the target. The results are printed and punched for subsequent plotting and listing.

(8) A *center of mass* section converts pion and proton data from proton-proton collisions to the center-of-mass frame.

(9) The *save carbon* section allows temporary storage of carbon cross-section results for later subtraction from CD_2 results to obtain deuterium cross sections.

(10) A *deuterium* section. This section takes the current foreground calculations (assumed to be a CD_2 run), subtracts the carbon cross section which had been saved, and divides by two to obtain the deuterium cross section. The inscattering corrections are not applied until after the deuterium cross sections have been extracted to avoid improper compounding of the errors.

*Work supported by the U. S. Atomic Energy Commission.

†Present address: National Accelerator Laboratory, P. O. Box 500, Batavia, Illinois.

¹R. Haddock, M. Zeller, and K. Crowe, UCLA Report No. UCLA-34P106 (unpublished).

²E. Heer *et al.*, in *Proceedings of the Williamsburg Conference on Intermediate Energy Physics*, edited by H. Funsten *et al.* (College of William and Mary, Williamsburg, Va., 1966), p. 277; W. Hirt, thesis, E. T. H. Zurich, 1968 (unpublished); W. Hirt *et al.*, CERN Report No. CERN 69-24 (unpublished).

³B. Baldoni *et al.*, *Nuovo Cimento* **26**, 1376 (1962).

⁴V. M. Guzhavin, G. K. Kliger, V. Z. Kolganov, A. V. Lebedev, K. S. Marish, Yu. D. Prokoshkin, V. T. Smolyankin, A. P. Sokolov, L. Am. Soroko, and Ts'ui Wa-Ch'uang, *Zh. Eksp. Teor. Fiz.* **46**, 1245 (1964) [*Sov. Phys. JETP* **19**, 847 (1964)].

⁵D. V. Bugg, A. J. Oxley, J. A. Zoll, J. G. Rushbrooke, V. E. Barnes, J. B. Kinson, W. P. Dodd, G. A. Doran, and L. Riddiford, *Phys. Rev.* **133**, B1017 (1964).

⁶B. S. Neganov and O. V. Savchenko, *Zh. Eksp. Teor.*

Fiz. **32**, 1265 (1957) [*Sov. Phys. JETP* **5**, 1033 (1957)].

⁷M. G. Meshcheriakov, V. P. Zrellov, B. S. Neganov, I. K. Vzorov, and A. F. Shabudin, *Zh. Eksp. Teor. Fiz.* **31**, 45 (1956) [*Sov. Phys. JETP* **4**, 60 (1957)].

⁸A. G. Meshkovskii, Iu. S. Pligin, Ia. Ia. Shalamov, and V. A. Shebanov, *Zh. Eksp. Teor. Fiz.* **31**, 560 (1956) [*Sov. Phys. JETP* **4**, 404 (1957)].

⁹V. M. Siderov, *Zh. Eksp. Teor. Fiz.* **31**, 178 (1956) [*Sov. Phys. JETP* **4**, 22 (1957)].

¹⁰Yu. A. Batusov, N. I. Kostanashvilli, G. I. Lebedich, D. S. Nabichwrishwilli, V. A. Yarba, *Yad. Fiz.* **10**, 805 (1969) [*Sov. J. Nucl. Phys.* **10**, 465 (1970)].

¹¹E. Lillethun, *Phys. Rev.* **125**, 665 (1962).

¹²M. G. Meshcheriakov, I. K. Vzorov, V. P. Zrellov, B. S. Neganov, and A. F. Shabudin, *Zh. Eksp. Teor. Fiz.* **31**, 55 (1956) [*Sov. Phys. JETP* **4**, 79 (1957)].

¹³A. G. Meshkovskii, Iu. S. Pligin, Ia. Ia. Shalamov, and V. A. Shebanov, *Zh. Eksp. Teor. Fiz.* **31**, 987 (1956) [*Sov. Phys. JETP* **4**, 842 (1957)]; *ibid.* **32**, 1328 (1957) [*Sov. Phys. JETP* **5**, 1085 (1957)].

¹⁴A. G. Meshkovskii, Ia. Ia. Shalamov, and V. A. Shebanov, *Zh. Eksp. Teor. Fiz.* **33**, 602 (1957) [*Sov. Phys.*

- JETP 6, 463 (1958)].
- ¹⁵A. G. Meshkovskii, Ia. Ia. Shalamov, and V. A. Shebanov, *Zh. Eksp. Teor. Fiz.* 34, 1426 (1958) [*Sov. Phys. JETP* 34, 987 (1958)].
- ¹⁶M. Gell-Mann and K. Watson, *Ann. Rev. Nucl. Sci.* 4, 219 (1970).
- ¹⁷S. Mandelstam, *Proc. Roy. Soc. (London)* A244, 491 (1958).
- ¹⁸S. J. Lindenbaum and R. H. Sternheimer, *Phys. Rev.* 105, 1874 (1969).
- ¹⁹M. E. Schillaci, R. R. Silbar, and J. Young, *Phys. Rev.* 179, 1539 (1969).
- ²⁰C. T. Grant, M. E. Schillaci, and R. R. Silbar, *Phys. Rev.* 184, 1737 (1969).
- ²¹D. Drechsel and H. J. Weber, *Nucl. Phys.* B25, 159 (1970).
- ²²H. W. Bertini and M. P. Guthrie, *Nucl. Phys.* A169, 670 (1971); B25, 670 (1971).
- ²³N. Metropolis, R. Bivins, M. Storm, Anthony Turkevich, J. M. Miller, and G. Friedlander, *Phys. Rev.* 110, 185 and 204 (1958).
- ²⁴B. Margolis, *Nucl. Phys.* B4, 433 (1968).
- ²⁵E. Ferrari and F. Selleri, *Nuovo Cimento* 21, 1028 (1961).
- ²⁶V. C. Suslenko and V. I. Kochkin, JINR report, Dubna, 1970 (unpublished).
- ²⁷M. Sternheim, private communication.
- ²⁸F. Selleri, *Nuovo Cimento* 40A, 236 (1965).
- ²⁹H. L. Anderson, M. S. Dixit, H. J. Evans, K. A. Klare, D. A. Larson, M. V. Sherbrook, R. L. Martin, D. Kessler, D. E. Nagle, H. A. Thiessen, C. K. Hargrove, E. P. Hincks, and S. Fukui, *Phys. Rev. D* 3, 1536 (1971).
- ³⁰Tsu Yao, *Phys. Rev.* 134, B454 (1964).
- ³¹M. E. Schillaci and R. R. Silbar, *Phys. Rev. D* 2, 1220 (1970).
- ³²R. Bivins and J. Wooten, private communication.
- ³³M. Sternheim and R. Silbar, following paper, *Phys. Rev. D* 6, 3117 (1972).
- ³⁴D. Beder, *Can. J. Phys.* 49, 1448 (1971).
- ³⁵H. Bakker and E. Segrè, *Phys. Rev.* 81, 489 (1951).
- ³⁶J. Hine and E. Brownell, *Radiation Dosimetry* (Academic, New York, 1956), p. 38.
- ³⁷J. Janni, Report No. AFWL-TR-65-150, Air Force Weapons Laboratory, Kirtland Air Force Base, New Mexico, 1966 (unpublished).
- ³⁸J. B. Cumming, *Ann. Rev. Nucl. Sci.* 13, 261 (1963).
- ³⁹J. B. Marion and B. A. Zimmerman, *Nucl. Instr. Meth.* 51, 93 (1967).